

## MIT Open Access Articles

### *Modeling and Optimization of Superhydrophobic Condensation*

The MIT Faculty has made this article openly available. **Please share** how this access benefits you. Your story matters.

**Citation:** Miljkovic, Nenad, Ryan Enright, and Evelyn N. Wang. "Modeling and Optimization of Superhydrophobic Condensation." *Journal of Heat Transfer* 135, no. 11 (November 1, 2013): 111004.

**As Published:** <http://dx.doi.org/10.1115/1.4024597>

**Publisher:** ASME International

**Persistent URL:** <http://hdl.handle.net/1721.1/84986>

**Version:** Author's final manuscript: final author's manuscript post peer review, without publisher's formatting or copy editing

**Terms of use:** Creative Commons Attribution-Noncommercial-Share Alike



# Modeling and Optimization of Superhydrophobic Condensation

Nenad Miljkovic,<sup>†</sup> Ryan Enright,<sup>†,‡</sup> and Evelyn N. Wang<sup>†,\*</sup>

<sup>†</sup>Department of Mechanical Engineering, Massachusetts Institute of Technology,  
77 Massachusetts Avenue, Cambridge, Massachusetts 02139, USA

<sup>‡</sup>Stokes Institute, University of Limerick, Limerick, Ireland

\*Address correspondence to enwang@mit.edu

**Keywords:** Superhydrophobic condensation, jumping droplets, droplet coalescence, condensation optimization, environmental scanning electron microscopy; micro/nanoscale water condensation, condensation heat transfer

## Abstract:

Superhydrophobic micro/nanostructured surfaces for dropwise condensation have recently received significant attention due to their potential to enhance heat transfer performance by shedding water droplets *via* coalescence-induced droplet jumping at length scales below the capillary length. However, achieving optimal surface designs for such behavior requires capturing the details of transport processes that is currently lacking. While comprehensive models have been developed for flat hydrophobic surfaces, they cannot be directly applied for condensation on micro/nanostructured surfaces due to the dynamic droplet-structure interactions. In this work, we developed a unified model for dropwise condensation on superhydrophobic structured surfaces by incorporating individual droplet heat transfer, size distribution, and wetting morphology. Two droplet size distributions were developed, which are valid for droplets undergoing coalescence-induced droplet jumping, and exhibiting either a constant or variable contact angle droplet growth. Distinct emergent droplet wetting morphologies, Cassie jumping, Cassie non-jumping, or Wenzel, were determined by coupling of the structure geometry with the nucleation density and considering local energy barriers to wetting. The model results suggest a specific range of geometries (0.5 – 2  $\mu\text{m}$ ) allowing for the formation of coalescence-induced jumping droplets with a 190% overall surface heat flux enhancement over conventional flat dropwise condensing surfaces. Subsequently, the effects of four typical self-assembled monolayer promoter coatings on overall heat flux were investigated. Surfaces exhibiting coalescence-induced droplet jumping were not sensitive (< 5%) to the coating wetting characteristics (contact angle hysteresis), which was in contrast to surfaces relying on gravitational droplet removal. Furthermore, flat surfaces with low promoter coating contact angle hysteresis (< 2°) outperformed structured superhydrophobic surfaces when the length scale of the structures was above a certain size (> 2  $\mu\text{m}$ ). This work provides a unified model for dropwise condensation on micro/nanostructured superhydrophobic surfaces and offers guidelines for the design of structured surfaces to maximize heat transfer.

## 1. Introduction

Dropwise condensation has received significant attention since its discovery in 1930 by Schmidt *et al.* [1], due to the superior heat transfer performance over conventional filmwise condensation [2-7]. The high performance enhancement of passive dropwise condensing surfaces is attributed to their ability to form discrete non-wetting droplets which, upon growing to a critical size ( $\sim 1$  mm), can shed from the surface by gravity, thereby reducing the overall thermal resistance compared to filmwise condensation. More recently, micro/nanostructured superhydrophobic surfaces have been investigated as potential dropwise condensing surfaces for energy conversion [8], atmospheric water harvesting [9, 10], and high heat flux thermal management applications [11] owing to the promise of further improvements in overall heat transfer performance compared to traditional dropwise condensation. Indeed, a recent study showed that when small droplets ( $\sim 10 - 100$   $\mu\text{m}$ ) merge on superhydrophobic structured surfaces, they can spontaneously jump *via* the release of excess surface energy independent of gravity [12]. This phenomenon is attributed to surface structuring, which enhances the hydrophobicity, and thereby decreases droplet pinning to the surface [13]. Droplet removal by this mechanism is highly desirable due to the increased number of small droplets [14] which efficiently transfer the majority of the heat from the surface [8, 15-17]. In addition, gravity independent droplet removal allows utilization of such surfaces in any orientation, unlike conventional passive condensing surfaces which require gravity for droplet removal, a severe limitation for mobile electronics and space applications [18]. Surface structuring may therefore be an ideal method to enhance condensation heat transfer.

While several groups have demonstrated that properly designed surfaces can enable stable superhydrophobic condensation [19-23], a unified modeling framework to optimize structure design that captures the dynamic phase change process is lacking [24]. The early dropwise condensation model of Le Fevre and Rose [25, 26] combined individual droplet heat transfer with droplet size distribution theory. Advanced models have since followed this work by including more accurate expressions for the growth of small droplets. Tanaka [27] used population balance theory to evaluate the local droplet size by taking into account the two mechanisms of growth: direct vapor accommodation onto the droplet and coalescence with neighboring droplets. As a result, better predictions of the droplet size distribution for small non-coalescing droplets were obtained. Abu-Orabi [28] further refined the dropwise condensation model by considering all possible thermal resistances associated with the droplet. More recently, the work of Kim and Kim [29] extended the previous models by determining more accurately the conduction resistance for droplets exhibiting large contact angles ( $\theta > 90^\circ$ ).

Despite significant developments on dropwise condensation modeling, predictive models for condensation on micro/nanostructured superhydrophobic surfaces are still lacking. Specifically, three main inconsistencies arise when applying previous models to condensation on structured surfaces: 1) Droplet wetting morphology cannot be predicted (*i.e.*, Cassie [30], Wenzel [31], suspended [24], or partially wetting [24, 32]), 2) Droplet contact angle can vary during droplet growth [14, 32, 33], and 3) Droplet size distribution is not valid for droplets with non-constant contact angles and with surfaces undergoing coalescence-induced droplet jumping as the main mode of droplet removal.

This work develops a model framework to predict dropwise condensation heat transfer for micro/nanostructured superhydrophobic surfaces. Pillar arrays, spanning a wide range of dimensions ( $\sim 10$  nm – 10  $\mu$ m), are utilized as the model structured surface. The current model incorporates prediction capability for the emergent droplet wetting morphology (Section 2), accounts for non-constant contact angle droplet growth (Section 3), and extends the previously developed droplet size distribution theory to both constant and non-constant contact angle droplets growing on surfaces experiencing coalescence-induced droplet jumping [12, 14] (Section 4). The results from the model are subsequently used to study the effects of surface structure design and size scale (Section 6), surface inclination (Section 7), and contact angle hysteresis with different promoter coatings (Section 8) on overall surface heat transfer. Optimization of the structure geometry indicates that surfaces with nanometer length scales and high nucleation densities have the potential to enhance overall condensation heat transfer performance by 190% when compared to conventional flat dropwise condensing surfaces. The outcomes of this work create important regime maps and design guidelines for highly efficient superhydrophobic condensation surfaces.

## 2. Droplet Wetting Morphology Model

During dropwise condensation on a structured superhydrophobic surface, droplets can depart either by coalescence-induced droplet jumping (if droplet/surface adhesion is small) or by gravity (if droplet/surface adhesion is large). The individual droplet contribution to the heat transfer process is highly sensitive to the droplet wetting morphology and therefore is necessary to predict the overall surface heat transfer by dropwise condensation.

To study the effects of surface structure geometry on emergent condensing droplet wetting morphology, we consider a model structured surface consisting of a micro/nanopillar array with heights  $h$ , diameters  $d$ , and pillar-to-pillar spacings  $l$  (solid fraction  $\phi = \pi d^2/4l^2$  and roughness factor  $r = 1 + \pi dh/l^2$ ) (Fig. 1(a) and (b)). To achieve superhydrophobicity, the model surface is assumed to be coated with a promoter film such as a self-assembled-monolayer (SAM) having intrinsic advancing/receding contact angles of  $\theta_a / \theta_r$  [34, 35]. During condensation on a structured superhydrophobic surface, the condensing liquid droplets can exhibit three distinct wetting morphologies: suspended (S) where condensed droplets sit on top of the micro/nanostructure (Fig. 1(c)) [30], partially wetting (PW) where the droplets form a liquid bridge connecting the base of the droplet (Fig. 1(d)) [24], or Wenzel (W) where droplets wet the cavities of the micro/nanostructure (Fig. 1(e)) [31].

To accurately predict the wetting morphology of a single droplet, a *non-equilibrium* thermodynamic energy criterion is used which emphasizes the role of contact line pinning on the resultant droplet morphology [22]. By comparing the dimensionless energy of the advancing Wenzel ( $\cos \theta_a^W = r \cos \theta_a$ ) [31] and Cassie ( $\cos \theta_a^{CB} = -1$ ) [36] droplet morphologies, the expected morphology can be estimated by

$$E^* = \frac{\cos \theta^{CB}}{\cos \theta^W} = \frac{-1}{r \cos \theta_a}. \quad (1)$$

When  $E^* > 1$  the contact line can overcome the energy barrier to de-pin and a W droplet is formed (Fig. 1(e)). If  $E^* < 1$  complete de-pinning is not possible and the droplet grows upwards over the top of the pillar array forming a PW Cassie droplet (Fig. 1(c), (d)).

Droplet coalescence introduces a further length scale dependency on the emergent droplet wetting morphology. When the average condensing droplet spacing  $\langle l_c \rangle$  approaches that of the pillar spacing  $l$  ( $\langle l_c \rangle \sim l$ ), the formation of local pinning barriers is disrupted. While it may be energetically favourable to form Cassie droplets ( $E^* < 1$ ), this may not be possible due to droplet coalescence between two adjacent unit cells which bypasses the pinning barriers associated with the pillar sides. This effect results in the formation of thermodynamically-unfavourable W droplets which are highly pinned to the surface. To avoid formation of W droplets on CB stable surfaces, a critical droplet separation distance of at least  $\langle l_c \rangle \geq 2l$  must be maintained [22].

For the purposes of this model, condensation on the structured surface is assumed to be spatially random. The mean condensing droplet spacing  $\langle l_c \rangle$  can be related to the nucleation density  $N_s$  by [24]

$$\langle l_c \rangle = \frac{1}{\sqrt{4N_s}}. \quad (2)$$

These two wetting criteria (Eqs. (1), (2)) have been validated experimentally for a wide variety of structured surfaces with a range of length scales and surface energies [2, 4, 22, 24]. The criteria form the basis for determining the emergent condensing droplet morphology on the micro/nanostructured surface. However, to gain an understanding of overall surface condensation performance, the individual droplet heat transfer for each morphology needs to be incorporated.

### 3. Droplet Heat Transfer Model

To accurately model dropwise condensation on micro/nanostructured surfaces, individual droplet growth rates and heat transfer are needed. The growth behavior of each droplet morphology can be obtained by modifying the Kim and Kim model [29] to account for the pillar geometry and emergent droplet morphology [24]. It is important to note that most previous models assume a constant droplet contact angle,  $\theta$ , during growth. This assumption is appropriate for dropwise condensation on flat hydrophobic surfaces [28, 29, 37], however, it does not apply for structured superhydrophobic surfaces, since droplets have been observed to have variable contact angles during growth [14, 18, 24, 32, 33, 38]. To resolve this discrepancy, a model was developed to predict the droplet contact angle  $\theta$  as a function of the droplet radius  $R$ .

#### 3.1 Contact Angle Modeling

The droplet contact angle  $\theta$  was modeled as a function of the droplet wetting morphology (PW, W, or S) and droplet radius  $R$ . When the droplet radius  $R$  is lower than the structure scale ( $R < l$ ), the droplet is assumed to have the intrinsic hydrophobic surface coating contact angle  $\theta_0$ . When the droplet grows to a size comparable to the structure scale ( $R \sim l$ ), it begins to interact with the pillars confining it and fills the unit cell to the top of the structures. At this point, depending on the energy criterion  $E^*$  and nucleation density  $N_s$ , the droplet can propagate above the unit cell and form a PW droplet, or it can propagate laterally and form a W droplet (Section 2). In addition, due to the spatially random nature of nucleation, droplets nucleating on Cassie stable surfaces can do so on the tips of pillars to form S droplets.

The PW droplet contact angle was modeled as a linear function of droplet radius  $R$  which has been shown to be a valid approximation [2, 4, 24]. Previous experimental studies using ESEM and optical microscopy (OM) revealed the characteristic diameter of the pinned neck of the condensing PW droplets is approximately  $2 \times 2$  unit cells [22, 24]. At later times, the PW droplet has an increasingly large apparent contact angle  $\theta_{PW}$  characteristic of the Cassie morphology (Fig. 2(a)) [2, 24].

Wenzel and S droplets are modelled as having a constant contact angle characteristic of the W and S morphologies (Figs. 2(b)-(c)). Although previous studies have shown that the W contact angle oscillates about some mean value with an amplitude as high as  $\sim 15^\circ$  at length scales ( $R/l \sim 1-3$ ), the oscillation amplitude will decay at larger sizes ( $R/l > 3$ ) as the droplet grows laterally during condensation [22]. Due to the relatively small amplitude of oscillation and its decay, we neglect the contact angle deviation to simplify the analysis. In addition, the magnitude of the W droplet contact angle oscillation ( $\sim 1 - 15^\circ$ ) is less than that of the PW droplet variable contact angle difference which can approach  $90^\circ$ .

The contact angle behavior of the PW, W, and S droplet morphologies can be summarized by:

$$\theta_{PW}(R) = \begin{cases} \theta_a, & R \leq l \\ \frac{\pi}{2} + \frac{(\theta_a^{CB} - \frac{\pi}{2})}{(R_{max} - l)}(R - l), & l < R < R_{max} \\ \theta_a^{CB}, & R \geq R_{max} \end{cases} \quad (3)$$

$$\theta_W(R) = \begin{cases} \theta_a, & R \leq l \\ \theta_a^W, & R > l \end{cases} \quad (4)$$

$$\theta_S(R) = \theta_a^{CB}, \quad (5)$$

where  $\cos \theta_a^{CB} = \varphi(\cos \theta_a + 1) - 1$ ,  $R_{max} = l / \sin(\pi - \theta_a^{CB})$  and  $\cos \theta_a^W = r \cos \theta_a$ .

### 3.2 Droplet Growth Modeling

At the scales considered in this work ( $\sim 1 \mu\text{m}$ ), the dominant mode of droplet growth is due to the direct accommodation of vapor molecules at the droplet interface [39]. For a droplet with radius  $R(t)$  on a structured superhydrophobic surface (Fig. 2(a)), the contact angle  $\theta$  varies with the droplet radius according to Eqs. (3)-(5). The local vapor ( $T_{sat}$ ) and surface ( $T_s$ ) temperatures are assumed to be constant throughout the growth process. The individual droplet heat transfer,  $q$ , is determined by considering all thermal resistances from the saturated vapor through the condensing droplet to the substrate (Fig. 3). All thermal resistances associated with the droplet are presented in terms of individual temperature drops: the liquid-vapor interfacial resistance due to direct vapor molecule accommodation at the droplet interface ( $\Delta T_i$ ), the conduction resistance through the droplet ( $\Delta T_d$ ), the conduction resistance through the pillars ( $\Delta T_{P,S}$ ) or liquid bridge and pillars ( $\Delta T_{P,PW}$ ), the promoter coating resistance ( $\Delta T_{HC}$ ), and the resistance due to the curvature of the droplet ( $\Delta T_C$ ). Internal droplet convection was neglected in the model since the droplets were sufficiently small so that conduction is the primary mode of heat transfer through the droplet [27, 40].

The temperature drop due to droplet curvature ( $\Delta T_C$ ) is given by [41]

$$\Delta T_C = \frac{R_{min}}{R} (T_{sat} - T_s) = \frac{2T_{sat}\sigma}{Rh_{fg}\rho_w}, \quad (6)$$

where  $T_{sat}$  is the water vapor saturation temperature,  $\sigma$  is the water surface tension,  $h_{fg}$  is the latent heat of vaporization,  $\rho_w$  is the liquid water density, and  $R_{min}$  is the droplet nucleation radius ( $R_{min} = 2T_{sat}\sigma/h_{fg}\rho\Delta T$ ).

The temperature drop between the saturated vapor and liquid interface ( $\Delta T_i$ ) is given by

$$\Delta T_i = T_{sat} - T_i = \frac{q}{h_i 2\pi R^2 (1 - \cos \theta)}, \quad (7)$$

where  $q$  is the heat transfer rate through the droplet and  $h_i$  is the condensation interfacial heat transfer coefficient given by [42, 43]

$$h_i = \frac{2\alpha}{2-\alpha} \frac{1}{\sqrt{2\pi R_g T_s}} \frac{h_{fg}^2}{v_g T_s}, \quad (8)$$

where  $R_g$  is the specific gas constant and  $v_g$  is the water vapor specific volume. The condensation coefficient  $\alpha$  is the ratio of vapor molecules that will be captured by the liquid phase to the total number of vapor molecules reaching the liquid surface (ranging from 0 to 1).

Once the vapor condenses on the droplet interface, the latent heat must be conducted through the droplet to the substrate. This resistance is modeled as a pure conduction resistance which leads to a temperature drop ( $\Delta T_d$ ) given by [29]

$$\Delta T_d = T_i - T_{b1} = \frac{q\theta}{4\pi R k_w \sin \theta}, \quad (9)$$

where  $T_{b1}$  is the liquid temperature of the droplet base (Fig. 3(b)) and  $k_w$  is the condensed water thermal conductivity. The temperature drop due to the promoter coating is calculated using a conduction resistance given by

$$\Delta T_{HC} = T_{b1} - T_{b2} = \frac{q\delta_{HC}}{\varphi\pi R^2 k_{HC} \sin^2 \theta}, \quad (10)$$

where  $T_{b2}$  is the temperature of the silicon pillars beneath the coating (Fig. 3(b)),  $\delta_{HC}$  is the coating thickness,  $\varphi$  is the structured surface solid fraction, and  $k_{HC}$  is the coating thermal conductivity.

The conduction resistance through the pillars is dependent on the wetting morphology of the droplet. For the S morphology, the temperature drop associated with the conduction resistance is given by

$$\Delta T_{P,CB} = T_{b2} - T_s = \frac{qh}{\varphi\pi R^2 k_p \sin^2 \theta}, \quad (11)$$

where  $T_s$  is the substrate temperature, and  $k_p$  is the pillar thermal conductivity.

For PW droplets, the conduction resistance temperature drop through the pillar and coating structure is calculated by considering a parallel heat transfer pathway from the base of the droplet to the substrate surface (Fig. 3(c)) given by

$$\Delta T_{P2} = T_{b1} - T_s = \frac{q}{\pi R^2 k_{HC} \sin^2 \theta} \left[ \frac{k_P \varphi}{\delta_{HC} k_P + h k_{HC}} + \frac{k_w(1-\varphi)}{\delta_{HC} k_w + h k_{HC}} \right]^{-1}, \quad (12)$$

It is important to note that the PW conduction temperature drop given by Eq. (12) becomes the S temperature drop when  $k_w = 0$  W/mK. In this case, there is no liquid bridge available for heat flow.

Accounting for all of the temperature drops, the individual droplet heat transfer rate is

$$q(R, \theta) = \frac{\pi R^2 \left( \Delta T - \frac{2T_{sat}\sigma}{Rh_{fg}\rho_w} \right)}{\frac{1}{2h_i(1-\cos\theta)} + \frac{R\theta}{4k_w \sin\theta} + \frac{1}{k_{HC} \sin^2 \theta} \left[ \frac{k_P \varphi}{\delta_{HC} k_P + h k_{HC}} + \frac{k_w(1-\varphi)}{\delta_{HC} k_w + h k_{HC}} \right]^{-1}}, \quad (13)$$

The droplet heat transfer is related to the droplet growth rate ( $dR/dt$ ) by the latent heat of phase change

$$q(R, \theta) = \dot{m} h_{fg} = \rho_w h_{fg} \frac{dV}{dt} = \frac{\pi}{3} \rho_w h_{fg} \frac{d}{dt} [(1 - \cos \theta)^2 (2 + \cos \theta) R^3]. \quad (14)$$

Differentiating Eq. (14), we obtain an explicit term for  $dR/dt$

$$q(R, \theta) = \pi \rho_w h_{fg} R^2 \frac{dR}{dt} \left\{ (1 - \cos^2 \theta) \sin \theta \frac{d\theta}{dR} R + (1 - \cos \theta)^2 (2 + \cos \theta) \right\}. \quad (15)$$

Equation (15) has been shown to have excellent agreement with experimental results for a variety of differing droplet morphologies including PW, S, W, and droplets growing on flat surfaces [2, 24]. In order to determine the overall surface heat transfer performance, the individual droplet heat transfer must be combined with the morphology dependent droplet size distribution.

#### 4. Droplet Size Distribution Theory

On a flat hydrophobic surface, droplet nucleation and growth proceeds through two mechanisms: 1) direct (non-interacting) growth where droplets nucleate and grow on spatially random high energy sites by direct deposition from the vapor onto the droplet surface [22], and 2) coalescence-dominated growth where the distances between neighboring droplets ( $l_c$ ) become smaller and coalescence occurs until the droplet is large enough to be swept off the surface by gravity [16]. The falling droplet is able to sweep away the droplets beneath it and clean the condensing surface so that new droplets can re-nucleate. As a result of this droplet growth from nucleation to departure, a wide range of droplet sizes exist on the condensing surface [11, 29].

Due to the dynamic nature of droplet growth on structured superhydrophobic surfaces [22, 24], the flat surface growth and departure mechanisms are not adequate to accurately predict the droplet size distribution. Three main inconsistencies arise: 1) Droplet departure on structured superhydrophobic surfaces may occur *via* coalescence-induced droplet jumping as size scales well below the capillary length; 2) Droplets can have a range of wetting morphologies (Fig. 1(c)-(e)) depending on the structure geometry and size scale (Section 2); and 3) Droplet contact angles may not be constant during growth depending on the emergent droplet wetting morphology (Section 3.1). In



light of these differences, new morphology dependent droplet size distributions were derived that are valid for structured superhydrophobic surfaces.

#### 4.1 Wenzel (W) and Flat Hydrophobic Surface Droplet Size Distribution

Structured superhydrophobic surfaces exhibiting W droplet growth have a droplet size distribution analogous to that of a flat hydrophobic surface. W droplets grow and merge until reaching a size characteristic of the capillary length before being swept off by gravity. Sweeping droplets roll down the surface and remove all droplets in their path, cleaning the condensing surface for new droplets to re-nucleate. The droplet sweeping mechanism allows for small, more effective, droplets to populate the surface and thereby minimizes the condensation heat transfer resistance. Due to the significant droplet/surface adhesion exhibited by W droplets, coalescence-induced droplet removal is not possible, rather gravity assisted sweeping of droplets from the surface dominates [12, 14, 22, 24].

For small W droplets undergoing non-interacting growth, the population balance theory can be used to determine the droplet size distribution [27-29]. The steady state W droplet size distribution is determined from the conservation of number of droplets entering a size range containing droplets with radii  $R_1$  to  $R_2$ , *i.e.*, the number of droplets entering this size range must equal to the number of droplets leaving. The W droplet growth rate is defined as

$$G = \frac{dR}{dt}. \quad (16)$$

The number of droplets entering the size range ( $R_1$ - $R_2$ ) in a time increment  $dt$  is  $An_1G_1dt$ , where  $A$  is the surface area and  $n_1$  represents the number of droplets of size  $R_1$ . Similarly, the number of droplets leaving the size range is  $An_2G_2dt$ . The number of droplets swept off the surface by droplet shedding is equal to  $Sn_{1-2}dRdt$ , where  $S$  is the sweeping rate at which the substrate surface is renewed by falling droplets, and  $n_{1-2}$  is the average population density in the size range. Applying droplet conservation, we obtain [28, 29]:

$$An_1G_1dt = An_2G_2dt + Sn_{1-2}dRdt. \quad (17)$$

In the limit of  $dR$  approaching zero, Eq. (17) can be reduced to

$$\frac{d(Gn)}{dR} + \frac{n}{\tau} = 0, \quad (18)$$

where  $\tau$  is the sweeping period ( $\tau = A/S$ ).

The solution to Eq. (18) can be determined by first solving for the droplet growth rate  $G$ . Relating the latent heat of phase change (Eq. (15)) to the individual droplet growth (Eq. (13)),  $G$  for W droplets is

$$G = \frac{1}{\rho_w h_{fg} (1 - \cos \theta)^2 (2 + \cos \theta)} \frac{\Delta T - \frac{2T_{sat}\sigma}{Rh_{fg}\rho_w}}{\frac{1}{2h_i(1 - \cos \theta)} + \frac{R\theta}{4k_w \sin \theta} + \frac{1}{k_{HC} \sin^2 \theta} \left[ \frac{k_P \phi}{\delta_{HC} k_P + h k_{HC}} + \frac{k_W (1 - \phi)}{\delta_{HC} k_W + h k_{HC}} \right]^{-1}}. \quad (19)$$

$$G = A_1 \frac{1 - \frac{R_{min}}{R}}{A_2 R + A_3}, \quad (20)$$

where

$$A_1 = \frac{\Delta T}{h_{fg} \rho_w (1 - \cos \theta)^2 (2 + \cos \theta)}, \quad (21)$$

$$A_2 = \frac{\theta}{4k_w \sin \theta}, \quad (22)$$

$$A_3 = \frac{1}{2h_i (1 - \cos \theta)} + \frac{1}{k_{HC} \sin^2 \theta} \left[ \frac{k_P \varphi}{\delta_{HC} k_P + h k_{HC}} + \frac{k_w (1 - \varphi)}{\delta_{HC} k_w + h k_{HC}} \right]^{-1}. \quad (23)$$

Solving Eq. (18) analytically, we obtain an expression for  $n(R)$  which is identical for growth of non-interacting droplets on a flat hydrophobic surface [29]. Note that in this case,  $W$  droplets are assumed to grow with constant apparent contact angles, making the analysis analogous to droplet condensation on a flat hydrophobic surface.

For large coalescing droplets, the droplet size distribution  $N(R)$  was established by Glicksman and Rose [25, 26],

$$N(R) = \frac{1}{3\pi R^2 \hat{R}} \left( \frac{R_e}{\hat{R}} \right)^{-\frac{2}{3}}, \quad (24)$$

where  $\hat{R}$  is the average maximum droplet radius (departure radius), and  $R_e$  is the radius when droplets growing by direct vapor addition begin to merge and grow by droplet coalescence.  $\hat{R}$  can be estimated by a force balance on the droplet contact line between gravity,  $F_g = (2 - 3 \cos \theta_e + \cos^3 \theta_e) \pi \hat{R}^3 \rho g \cos \theta / 3$ , and surface tension,  $F_\sigma = 2\sigma \hat{R} \sin \theta_e (\cos \theta_r - \cos \theta_a)$ , given by [44, 45]

$$\hat{R} = \left[ \frac{6(\cos \theta_r - \cos \theta_a) \sin \theta_e \sigma}{\pi(2 - 3 \cos \theta_e + \cos^3 \theta_e) \rho g \cos \theta} \right]^{\frac{1}{2}}, \quad (25)$$

where  $\theta_a$  and  $\theta_r$  are the apparent structured surface advancing and receding contact angles [36, 46],  $\theta_e$  is the apparent equilibrium contact angle  $\theta_e = \cos^{-1}(0.5 \cos \theta_a + 0.5 \cos \theta_r)$ , and  $\theta$  is the surface inclination from the vertical, *i.e.*,  $\theta = 0^\circ$  corresponds to a vertical condensing surface and  $\theta = 90^\circ$  corresponds to a horizontal surface.

The radius when droplets begin to merge on the surface  $R_e$  is determined by assuming the nucleation process is random (Poisson) [22, 24]. Relating  $R_e$  to the nucleation density, we obtain

$$R_e = \frac{l_c}{2} = \frac{1}{4\sqrt{N_S}}, \quad (26)$$

where  $l_c$  is the droplet coalescence length and  $N_S$  is the droplet nucleation density per unit area of condensing surface. It is important to note that the assumption of a random Poisson distribution of nucleation sites results in a droplet interaction radius that is half of the interaction radius if we assume a square array of nucleation sites [29].

The droplet size distribution (Eq. (18)) can be analytically solved for by assuming the non-interacting and large droplet size distributions are equal ( $n(R_e) = N(R_e)$ ). The solution is given by [29]

$$n(R) = \frac{1}{3\pi R^2 \hat{R}} \left(\frac{R_e}{\hat{R}}\right)^{-\frac{2}{3}} \frac{R(R-R_{min})}{R-R_{min}} \frac{A_2 R + A_3}{A_2 R_e + A_3} \exp(B_1 + B_2), \quad (27)$$

where

$$B_1 = \frac{A_2}{\tau A_1} \left[ \frac{R_e^2 - R^2}{2} + R_{min}(R_e - R) - R_{min}^2 \ln \left( \frac{R - R_{min}}{R_e - R_{min}} \right) \right], \quad (28)$$

$$B_2 = \frac{A_2}{\tau A_1} \left[ R_e - R - R_{min} \ln \left( \frac{R - R_{min}}{R_e - R_{min}} \right) \right], \quad (29)$$

$$\tau = \frac{3R_e^2 (A_2 R_e + A_3)^2}{A_1 (11A_2 R_e^2 - 14A_2 R_e R_{min} + 8A_3 R_e - 11A_3 R_{min})}. \quad (30)$$

Figure 4 shows the droplet size distribution  $n(R)$  as a function of droplet radius  $R$ . The distribution at small droplet sizes (colored lines) ( $R < R_e$ ) is approximately constant since droplets do not interact with each other. In addition, smaller droplets have the highest population density due renewal of the surface by the droplet sweeping mechanism. In contrast, coalescing droplets (black line) ( $R > R_e$ ) have a reduced population density because both sweeping and coalescence acts to remove them from the surface [28, 29].

## 4.2 Suspended (S) Droplet Size Distribution

The growth and departure process of S droplets on a structured surface differs markedly from that of W droplets. A recent study showed that when small S and PW droplets (~10 - 100  $\mu\text{m}$ ) merge on superhydrophobic structured surfaces, they can spontaneously jump *via* the release of excess surface energy independent of gravity [12]. Droplet removal by this mechanism is highly desirable due to the increased number of small droplets [14] which efficiently transfer the majority of the heat from the surface [8, 15, 16]. However, if the surface solid fraction is too high ( $\phi \gtrsim 0.1$ ), coalescence-induced droplet jumping is not observed due to higher droplet surface adhesion. It is important to note that the chosen cutoff ( $\phi \approx 0.1$ ) for droplet jumping is a representative estimate and may not be exact. In addition, the role of apparent contact angle  $\theta$  on droplet jumping is currently not well understood, and is not considered in this model. In reality, a droplet jumping stable surface may exist where jumping is not possible for low apparent contact angles ( $l_c/l \rightarrow 2$ ), but may exist for larger apparent contact angles ( $l_c/l \rightarrow \infty$ ) on the same surface.

In order to model the droplet size distribution, a similar approach to the W droplet model is used. Suspended droplets nucleating on the tips of a structured surface grow and, once reaching a size large enough to begin interacting, merge and are removed from the surface ( $\phi < 0.1$ ). This process makes the non-interacting growth mechanism dominant and the population balance theory valid for the entire growth range [24]. In addition, droplet sweeping is non-existent on a surface exhibiting coalescence-induced droplet departure due to the removal of small droplets before they reach the capillary length. Applying droplet conservation for a size range  $R_1 - R_2$ , we obtain:

$$An_{S1}G_1 dt = An_{S2}G_2 dt. \quad (31)$$

In the limit of  $dR$  approaching zero, Eq. (31) can be reduced to

$$\frac{d(Gn_S)}{dR} = 0. \quad (32)$$

In this case, since S droplets undergo growth with a constant contact angle, an analytical solution for the droplet size distribution can be obtained. Equations (19)-(23), which outline the derivation of the droplet growth rate  $G$ , are valid in this case for S droplets. Applying the chain rule and integrating Eq. (32), we obtain

$$\int \frac{dn_S}{n_S} = \int \frac{A_2}{A_2R+A_3} dR - \int \frac{R_{min}}{R(R-R_{min})} dR. \quad (33)$$

For large coalescing droplets ( $R > R_e$ ),  $n(R) = 0$  due to the coalescence-induced droplet departure. The maximum droplet size  $\hat{R}$  for coalescence-induced jumping droplets is given by

$$\hat{R} = R_e = \frac{l_c}{2} = \frac{1}{4\sqrt{N_S}}. \quad (34)$$

The droplet size distribution (Eq. (33)) can be analytically solved by assuming the non-interacting and interacting droplet size distributions are equal ( $n(R) = N(R)$ ) at  $R = R_e$ . The solution is given by

$$n_S(R) = \frac{1}{3\pi R^2 \hat{R}} \left(\frac{R_e}{\hat{R}}\right)^{-\frac{2}{3}} \frac{R(R-R_{min})}{R-R_{min}} \frac{A_2R+A_3}{A_2R_e+A_3}, \quad (35)$$

The droplet size distribution ( $n_s(R)$ ) can be understood physically in terms of an asymptotic solution of the classical non-interacting droplet size distribution  $n(R)$  (Eq. (27)). By assuming the sweeping time approaches infinity ( $\tau \approx \infty$ ) or the sweeping frequency approaches zero ( $S \approx 0$ ); the sweeping mechanism is removed from the population balance analysis. Including this assumption for Eq. (27), the exponential term disappears and Eq. (35) is obtained. It is important to note, Eq. (35) is valid for any surface exhibiting coalescence-induced droplet departure where the droplet contact angle can be approximated as constant throughout the growth, and is not exclusively valid for S droplets only.

Figure 5(a) shows the droplet size distribution,  $n_s(R)$  as a function of droplet radius  $R$  for a variety of nucleation densities  $N_s$ . The three curves (solid lines) correspond to coalescence lengths of  $l_c = 10, 15$  and  $20 \mu\text{m}$ . The droplet size distribution is distinct from the derived solution for non-coalescence-induced droplet departing surfaces (Fig. 4). The results indicate that droplets larger than the coalescence length ( $R > R_e$ ) are non-existent, which is consistent with the physical interpretation of droplet departure due to coalescence. For all three cases, the distributions  $n_s(R)$  have a minimum at a droplet radius  $R \approx 1.2 \mu\text{m}$ . This result is due to the slower droplet growth for  $R < 1.2 \mu\text{m}$  caused by the increasing contribution from the droplet curvature resistance. As a consequence of the slower growth, the droplet population density is increased due to the conservation of droplets entering and leaving a droplet population. Droplets larger than  $R \approx 1.2 \mu\text{m}$  grow at a reduced rate due to increasing conduction thermal resistance through the droplet, therefore the droplet distribution increases with  $R$  up to the departure length

( $R = R_c = l_c/2$ ). In addition, the lack of a sweeping mechanism to remove small droplets allows for the overall population density to be higher than the classical case (Fig. 4).

### 4.3 Partially Wetting (PW) Droplet Size Distribution

In certain cases, droplets growing during condensation cannot be characterized by a constant contact angle  $\theta$  during growth, as in the case of PW droplets. Previous studies have shown that once PW droplets reach a size comparable to the structure ( $R \sim l$ ), they begin to undergo a growth regime where the contact angle varies while the basal area remains constant [14, 24, 32, 33, 38]. To capture this behavior in our model, a modified droplet size distribution was derived for surfaces undergoing variable contact angle droplet growth (PW).

Partially wetting droplets nucleate randomly on a structured surface, grow, and upon reaching a size large enough to begin interacting ( $R = R_c$ ), merge and are removed from the surface *via* coalescence-induced departure. Droplet sweeping is non-existent on this surface due to the removal of small droplets before they reach the capillary length. Applying droplet conservation for a size range  $R_1 - R_2$ , we obtain:

$$An_{d1}G_{pw1}dt = An_{d2}G_{pw2}dt . \quad (36)$$

where  $n_d$  is the ‘dynamic’ droplet size distribution for droplets undergoing variable contact angle growth (PW), and  $G_{pw}$  is the PW droplet growth rate  $G_{pw} = dR_{pw}/dt$ . The term ‘dynamic’ is used here due to the non-exclusiveness of this derivation to PW droplets only. This formulation can be applied to any droplet morphologies undergoing variable contact angle growth.

In the limit as  $dR$  approaches zero, Eq. (36) can be reduced to

$$\frac{d(G_{pw}n_d)}{dR} = 0 . \quad (37)$$

Since PW droplets grow with a variable contact angle, an analytical solution for the droplet size distribution  $n_d(R)$  cannot be obtained. In addition, Eqs. (19)-(23), which represent the droplet growth rate  $G_{pw}$  must be re-derived due to the contact angle variance (Section 3.1). The latent heat of phase change for PW droplets is expressed by

$$q_{pw}(R) = \pi\rho_w h_{fg} R^2 G_{pw} \left\{ (1 - \cos^2 \theta) \sin \theta \frac{d\theta}{dR} R + (1 - \cos \theta)^2 (2 + \cos \theta) \right\}. \quad (38)$$

By relating Eq. (38) to the droplet heat transfer Eq. (19), we can solve explicitly for  $G_{PW}$ :

$$G_{PW} = A_{1PW} \frac{1 - \frac{R_{min}}{R}}{A_2 R + A_3} , \quad (39)$$

where

$$A_{1PW} = \frac{\Delta T}{\rho_w h_{fg} \left\{ (1 - \cos^2 \theta) \sin \theta \frac{d\theta}{dR} R + (1 - \cos \theta)^2 (2 + \cos \theta) \right\}}. \quad (40)$$

Because  $G_{pw}$  is a function of  $R$  and  $\theta$ , Eq. (37) is first expanded and solved numerically. The differential equation to be solved is given by

$$\frac{dn_d}{dR} + \frac{1}{G_{pw}} \frac{dG_{pw}}{dR} n_d = 0. \quad (41)$$

The boundary condition for this case is identical to that of the S case, where the droplet size distribution at  $R = R_e$  is equal to the Rose distribution [25] given by

$$n_d(R_e) = N(R_e) = \frac{1}{3\pi R_e^2 \hat{R}} \left(\frac{R_e}{\hat{R}}\right)^{-\frac{2}{3}}, \quad (42)$$

where

$$\hat{R} = R_e = \frac{l_c}{2} = \frac{1}{4\sqrt{N_S}}. \quad (43)$$

Figure 5(a) shows the droplet size distribution,  $n_d(R)$  as a function of droplet radius  $R$  for a variety of nucleation densities. The three plotted curves (dashed lines) correspond to coalescence lengths of  $l_c = 10, 15$  and  $20 \mu\text{m}$ . The dynamic droplet size distribution varies from the ‘static’ or S solution (Eq. (35)). The plot indicates that inclusion of the droplet contact angle variability is important since the constant contact angle solution,  $n_s(R)$ , tends to overestimate the distribution by as much as 100% in some cases. Similar to  $n_s(R)$ , droplets larger than the coalescence length ( $R > R_e$ ) do not exist due to coalescence-induced droplet departure. In addition the distribution  $n_d(R)$  has a minimum identical to that of  $n_s(R)$  at a droplet radius  $R \approx 1.2 \mu\text{m}$  due to the curvature thermal resistance included in the growth model (see section 4.2).

To accurately predict the overall structured surface dropwise condensation heat transfer performance, the droplet size distributions derived in this section are combined with the individual droplet growth rates to determine the overall surface heat flux.

## 5. Overall Surface Heat Flux

The overall surface heat flux,  $q''$ , can be obtained at steady state by combining the morphology dependent individual droplet heat transfer rate (Eq. (13)) with the droplet size distributions (Eqns. (27), (35), and (41)). For flat hydrophobic surfaces or structured surfaces showing the W droplet morphology, the surface heat flux is given by

$$q_w'' = \int_{R_{min}}^{R_e} q(R)n(R)dR + \int_{R_e}^{\hat{R}} q(R)N(R)dR. \quad (45)$$

For structured surfaces showing the S droplet morphology, or coalescence-induced droplet departure with a static droplet contact angle, the surface heat flux is given by

$$q_s'' = \int_{R_{min}}^{R_e} q(R)n_s(R)dR. \quad (46)$$

For structured surfaces showing the PW droplet morphology, or surfaces exhibiting non-constant contact angle behavior, the surface heat flux is given by

$$q_d'' = \int_{R_{min}}^{R_e} q_{PW}(R) n_d(R) dR. \quad (47)$$

To compare the utility of the developed dynamic contact angle model, we determined the predicted surface heat flux ratio of the constant contact angle with the variable contact angle formulations for a surface undergoing PW droplet growth. Figure 5(b) shows the results of the comparison, indicating that the ‘static’ contact angle formulation is a good approximation for variable contact angle droplets at departure lengths larger than approximately 8  $\mu\text{m}$ . However, at smaller departure lengths, the static formulation deviates significantly from the dynamic solution, with error in excess of 50% at coalescence lengths below 2  $\mu\text{m}$ . Although the error is large at small length scales ( $R < 8 \mu\text{m}$ ), the static approximation works fairly well at larger coalescence lengths, showing the error to be within 10%.

In order to gain a better understanding of structured surface design, the dropwise condensation models developed were applied to an optimization scheme to examine the interplay between surface structure, droplet morphology, removal mechanisms and overall surface heat transfer performance.

## 6. Design and Optimization of Structured Surfaces

A number of recent works have fabricated superhydrophobic structured surfaces for the purpose of enhanced dropwise condensation *via* coalescence-induced droplet removal [10, 19-21, 23, 31, 47-50]. These surfaces were designed to be Cassie stable such that PW or S droplets are formed on micro/nanostructures [30] to have minimal contact line pinning. However, the design methodology of these surfaces is not very well understood. In an effort to provide a rational basis for structured surface design, prior to and post droplet departure, we utilized the newly developed model to evaluate the effects of surface geometry, scaling down the size scale of the structures, and intrinsic surface wettability (promoter coating) on overall heat transfer performance.

The droplet wetting morphology model was combined numerically with the growth rate and size distribution models. In the case of Cassie droplet formation, we assumed the PW morphology to emerge due to the use of smooth pillars and the ability of S droplets to transition to PW droplets [24]. This assumption was used to provide an upper bound for surface heat transfer performance when compared to conventional flat hydrophobic surfaces. Figure 6 shows the droplet contact angle  $\theta$  (Fig. 6(a)) and departure radius  $\hat{R}$  (Fig. 6(b)) as a function of structure geometry ( $d/l$ ) and coalescence length ( $l_c/l$ ). The results indicate distinct regions of droplet morphology in accordance to the wetting criteria outlined in Section 2. For  $d/l < 0.16$ , the W wetting morphology was favored due to the low energy barrier of liquid propagation in the lateral direction. At larger  $d/l$  ratios ( $0.16 < d/l < 0.36$ ), the Cassie (PW) morphology became favored with coalescence-induced jumping as the main mode of droplet removal. At even larger  $d/l$  ratios ( $d/l > 0.36$ ), the PW morphology remained favorable, however the coalescence-induced droplet jumping behavior significantly diminished in favor of conventional droplet sweeping due to high droplet surface pinning ( $\varphi > 0.1$ ).

Figure 6(a) show the dynamic nature of  $\theta$  for all three droplet morphologies (W, PW jumping, and PW shedding). At  $l_c/l < 2$  (not shown),  $\theta$  remains constant since the droplet radius is not large enough to fill the structure. In this regime, droplets grow individually within the unit cells and take on the intrinsic advancing contact angle,  $\theta_a$ .

Upon reaching a size comparable to  $2 \times 2$  unit cells ( $l_c/l = 2$ ), droplets begin to either 1) emerge from the structure and grow in the constant-basal-area / variable-contact-angle PW droplet mode ( $d/l > 0.16$ ) [2, 32, 38] or 2) spread laterally and grow in the constant contact angle W droplet mode ( $d/l < 0.16$ ). For the jumping region ( $0.16 < d/l < 0.36$ ),  $\theta$  increased with increasing  $l_c/l$  due to the differing droplet departure radii. The region of non-jumping PW droplets ( $d/l > 0.36$ ) showed constant  $\theta$  that decreased with increasing  $d/l$  due to increasing solid fraction  $\phi$ . The W regime ( $d/l < 0.16$ ) showed increased  $\theta$  with increasing  $d/l$  due to larger surface roughness  $r$ .

In addition to having a large influence on the droplet contact angle, the distinct regions of different droplet morphologies created a large variance in the droplet departure radius  $\hat{R}$  (Fig. 6(b)). The W regime had the highest  $\hat{R}$  due to the high contact angle hysteresis and droplet surface adhesion. W droplets rely on the gravitational force to be removed from the surface, reaching sizes comparable to the capillary length ( $\hat{R} \approx 2$  mm) before departing. In contrast, PW droplets exhibiting jumping behavior ( $0.16 < d/l < 0.36$ ) depart from the surface at length scales well below the capillary length ( $\hat{R} \ll 1$  mm). As  $d/l$  increased further ( $d/l > 0.36$ ), the PW non-jumping regime becomes favored. However, the departure radii of these non-jumping PW droplets are well below that of W droplets due to the significantly smaller contact angle hysteresis and droplet surface adhesion associated with the Cassie morphology. At coalescence lengths of  $l_c/l < 2$  (not shown), droplets merge within the structure to form liquid films and highly irregular W droplets that depart *via* gravitational shedding.

## 6.1 Optimization of Surface Heat Flux

The optimal dropwise condensation enhancement was determined based on the overall surface heat flux for a variety of structured surface geometries. Figure 7(a) shows the normalized surface condensation heat flux,  $q''/q_{\max}''$ , as a function structure geometry ( $d/l$ ) and coalescence length ( $l_c/l$ ). Distinct regions of operation exist due to varying droplet morphologies and their associated departure and contact angle characteristics (Fig. 6). As expected, the region favoring PW jumping droplets ( $0.16 < d/l < 0.36$ ) showed maximum heat flux for the entire range of  $l_c/l$ . Wenzel droplets ( $d/l < 0.16$ ) showed the lowest heat flux due to their relatively large departure radii indicating that structured surfaces having very low solid fractions can be far from optimal in terms of dropwise condensation performance. The regime of non-jumping PW droplet formation ( $d/l > 0.36$ ) showed a decrease in performance compared to the jumping regime. However at increased solid fractions ( $d/l > 0.8$ ), the heat flux became comparable due to favorable departure conditions and high droplet-base contact (high individual droplet growth rate prior to departure). The results indicate that an optimum structure geometry exists to maximize the overall surface heat flux, and that the unified model can be used to find this optimum. In this case, designing  $d/l$  to be within the range of  $0.16 < d/l < 0.36$  is highly favorable in terms of overall heat flux performance. However, this criteria may not hold for different surfaces, since the morphology is strongly dependent on the solid fraction and surface roughness.

## 6.2 Effect of Micro/Nanostructure Scale

Scaling down of the structured surface has been shown to potentially increase the overall performance due to the reduction in thermal resistance between the base of the emerging droplet and the structured surface substrate [2, 24]. To study the effects of structure scale on the overall surface heat transfer performance, the unified model was used



to simulate condensation on a surface having  $h/l = 2$  for a variety of different pillar heights  $h$ . Figures 7(a)-(c) show the normalized surface heat flux,  $q''/q_{\max}''$ , for pillar heights of  $h = 5 \mu\text{m}$ ,  $h = 2 \mu\text{m}$ , and  $h = 1 \mu\text{m}$ , respectively. The results show enhanced heat transfer performance (up to 22.5% from  $h = 5 \mu\text{m}$  to  $h = 1 \mu\text{m}$ ) for surfaces with smaller scale structures due to the reduced structure thermal resistance. In addition, reduction of the pillar height acts to extend the peak performance of the surface for a larger range of coalescence lengths ( $l_c/l$ ).

A second important advantage of scaling down the micro/nanostructure is seen by the broadening of the  $d/l$  ratio for the PW jumping regime. Figure 8 shows the structured surface steady-state wetting morphology as a function of the pillar diameter to center-to-center spacing ratio ( $d/l$ ) and the center-to-center spacing to pillar height ratio ( $l/h$ ). As  $l$  is reduced for a fixed  $h$ , the region of  $d/l$  where PW jumping droplets are favored expanded. This increase of the  $d/l$  range for PW jumping stability has very important implications for nanostructured surface design, since the structure can consist of highly irregular pillar type protrusions arising from non-uniform fabrication techniques such as oxidation [4] or self-assembly [33]. The larger range of  $d/l$  at smaller length scales facilitates tolerance of structure irregularity and imperfection, allowing for less costly, scalable, and robust fabrication techniques to be used [4].

Although the heat flux increases as the structure scale is decreased from micro to nano, the corresponding required coalescence lengths are also decreased. This effect may pose a problem in realistic structured surface design since the coalescence-induced droplet jumping mechanism has been shown to have a minimum size limit [12].

## 7. Intrinsic Contact Angle

Dropwise condensation of water on metal/metal oxide surfaces is rarely observed in natural conditions due to their high surface energies (the exception being noble metals such as gold and platinum due to adsorption of atmospheric hydrocarbons [51-53]). To promote dropwise condensation, the use of self-assembled monolayers (SAMs) has emerged as popular and robust technique to obtain reduced surface energies [4, 10, 12, 14, 19, 22-24, 29, 32, 38, 47, 54, 55]. The use of SAMs as surface promoter coatings has three advantages: 1) The SAM thickness is on the order of a few nanometers, resulting in minimal resistance to heat flow [29]; 2) A range of SAMs can form a covalent bond with metal oxide surfaces greatly increasing robustness; and 3) The highly non-wetting properties of fluorinated SAMs act as a suitable promoter for dropwise condensation. The developed model is utilized to quantify the effect of SAM coating properties for selecting an optimal dropwise condensation promoter.

Four chemistries for SAM formation were examined, with varying chain lengths and intrinsic contact angles on smooth surfaces. The advancing and receding contact angles used were:  $\theta_a / \theta_r = 121.6^\circ/86.1^\circ$ ,  $\theta_a / \theta_r = 110.8^\circ/85.8^\circ$ , and  $\theta_a / \theta_r = 103.8^\circ/102.7^\circ$  corresponding to typical wetting properties for deposited films of (tridecafluoro-1,1,2,2-tetrahydrooctyl)-1-trichlorosilane (SAM1), octadecyltrichlorosilane (SAM2), and dichlorodimethylsilane (SAM3), respectively [22]. In addition, a thiolated SAM coating (THIOL) was analysed with intrinsic advancing and receding contact angles of  $\theta_a / \theta_r = 121.1^\circ/106.3^\circ$ .

Figures 9(a) and (b) show the surface heat flux  $q''$  as a function of coalescence length  $l_c$  for a structured surface coated with the four coatings with (a)  $d/l = 0.3$  and (b)  $d/l = 0.4$ . While both surfaces favor formation of PW

droplets, Fig. 9(a) and (b) underwent coalescence-induced droplet jumping and gravity based droplet shedding, respectively. For all four coatings, as  $l_c$  decreased,  $q''$  increased due to the increase in population of small droplets ( $R < l_c$ ). The impact of the coatings on  $q''$  showed different sensitivity depending on the droplet morphology and departure mechanism. In the case of coalescence-induced droplet removal (Fig. 9(a)), the effect of intrinsic wetting angle (coating type) on  $q''$  was small. This result is due to the fact that droplets growing on the structured surface depart at length scales well below the capillary length ( $l_c \ll 1$  mm), where contact line hysteresis is very important in the removal mechanism of droplets from the surface.

When the droplet removal mechanism depends on gravity (Fig. 9(b)), the intrinsic wetting angle of the coating has a significant effect on  $q''$ . Droplets being removed by gravity need to grow to a size large enough to overcome the adhesive surface tension force. The adhesion force is highly dependent on contact angle hysteresis ( $\Delta\theta = \theta_a - \theta_r$ ) of the coating (Eq. (25)); the larger the hysteresis, the larger the adhesion to the surface [44, 45]. The lower the hysteresis, the smaller the pinning force and average droplet size before departure occurs, resulting in a larger population of smaller droplets and enhanced  $q''$ . Figure 9(b) shows that the smallest contact angle hysteresis coatings have the best performance (SAM3 has the best performance ( $\Delta\theta_{\text{SAM3}} = 1.1^\circ$ ) followed in order by THIOIOL ( $\Delta\theta_{\text{THIOIOL}} = 14.8^\circ$ ), SAM2 ( $\Delta\theta_{\text{SAM2}} = 25^\circ$ ), and SAM1 ( $\Delta\theta_{\text{SAM1}} = 35.5^\circ$ )).

## 8. Condensing Surface Orientation

Structured surfaces undergoing coalescence-induced droplet jumping can be utilized in a variety of applications where conventional flat hydrophobic surfaces (gravity based droplet shedding) cannot, including space, mobile electronics, and thermal diodes [18]. To study the effect of surface orientation on overall surface heat flux, the surface inclination angle,  $\theta$ , was varied from  $\theta = 0^\circ$  (vertical) to  $\theta = 90^\circ$  (horizontal) in the model. Figure 10 shows the surface heat flux as a function of the inclination angle for SAM coated structured surfaces exhibiting PW coalescence-induced droplet jumping ( $d/l = 0.3$ ) and PW gravity based droplet shedding ( $d/l = 0.4$ ). Surfaces exhibiting jumping showed little sensitivity to the surface orientation owing to their ability to shed droplets at length scales well below the capillary length ( $\hat{R} \ll 1$  mm). Although, in the horizontal orientation ( $\theta = 90^\circ$ ), jumping droplets can return to the surface *via* gravitational force and reduce heat transfer, this effect can be neglected due to the ease of small droplet ( $\sim 10$   $\mu\text{m}$ ) advection or entrainment in the bulk water vapor flow above the surface.

In contrast to jumping droplets, heat flux performance of surfaces exhibiting gravity based droplet shedding was reduced due to larger droplet departure size (Fig. 6(b)), and showed large sensitivity to surface orientation. The main mechanism of droplet removal in this case is highly dependent on the gravitational body force acting on the condensing droplets. Before they can be removed, droplets need to grow to a size large enough for gravity to overcome the contact line surface tension force holding them on to the surface. The surface tension force arises due to contact angle hysteresis and acts in a direction parallel with the surface substrate. Therefore, to maximize the gravitation force, the vertical surface orientation is highly favoured and any deviation towards the horizontal orientation results in a larger departing droplet size ( $\hat{R}$ ) and lower overall surface heat flux (particularly at inclination angles above  $30^\circ$ ). As expected, the SAM coatings with the smallest contact angle hysteresis have the

best performance (SAM1 has the worst performance ( $\Delta\theta_{\text{SAM1}} = 35.5^\circ$ ) followed in order by SAM2 ( $\Delta\theta_{\text{SAM2}} = 25^\circ$ ), and THIOL ( $\Delta\theta_{\text{THIOL}} = 14.8^\circ$ ).

## 9. Flat vs. Structured Surfaces

In an effort to address the question: can a flat hydrophobic surface with low contact angle hysteresis,  $\Delta\theta = \theta_a - \theta_r$ , outperform a structured superhydrophobic surface exhibiting droplet jumping, we used the developed model to compare the heat transfer of structured surfaces exhibiting a range of length scales ( $1 \mu\text{m} < h < 5 \mu\text{m}$ ,  $h/l = 2$ ) with flat hydrophobic surfaces with a range of intrinsic surface contact angle hysteresis values ( $0^\circ < \Delta\theta < 55^\circ$ ) (Fig. (11)). Figure 11 shows that as the contact angle hysteresis is reduced for a flat surface ( $\theta_a = 120^\circ$ ,  $\theta_r = \text{variable}$ ), the overall heat flux is increased due to the reduction in the required size of the droplet to overcome surface tension forces to initiate shedding (Fig. 11 Inset). In addition, the results show that at low enough contact angle hysteresis, the flat surface can potentially have better performance than a jumping superhydrophobic surface. However, as the length scale of the superhydrophobic surface is reduced, the required hysteresis to maintain enhancement is also reduced ( $\Delta\theta < 27^\circ$  for  $h = 5 \mu\text{m}$ ,  $\Delta\theta < 2.5^\circ$  for  $h = 2 \mu\text{m}$ ,  $\Delta\theta < 1^\circ$  for  $h = 1 \mu\text{m}$ ). This result is in accordance with the theory and subsequently the jumping surface heat fluxes are increased (Section 6.2). Therefore, structured surfaces with relatively large structure scale features may not be advantageous when compared to a flat hydrophobic surface. However, provided that the surface structure design is optimized (Fig. 7(c)) with low coalescence lengths ( $2 < l_c/l < 4$ ), the heat flux performance enhancement of peak superhydrophobic condensation ( $q_{\text{max}} = 342.12 \text{ kW/m}^2$  at  $\Delta T = 5 \text{ K}$ ) compared to that of an ideal flat surface ( $\Delta\theta < 2.5^\circ$ ) approaches 110%. In addition, using the model results to compare the peak superhydrophobic heat flux ( $q_{\text{max}}$ ) to a more realistic flat dropwise condensing surface (SAM1 coated) shows an even greater enhancement of up to 190%.

The results indicate that structured surfaces may be the ideal pathway to achieving even higher dropwise condensation heat fluxes over conventional flat hydrophobic surfaces. Such surfaces may therefore enable: 1) Substantial reduction in industrial condenser sizes and cost [51]; 2) Overall performance enhancement of devices such as heat pipes and thermal ground planes for applications requiring maximization of evaporator area and minimization of condenser area [56]; and 3) Use of cooling devices previously not possible for local high heat flux electronic devices [18, 57].

Although the added benefit of surface structuring may outweigh its increased complexity, some practical limitations remain. The scalability of the surface structuring process is a concern that has to be addressed before practical designs are implemented in industrial settings. Recent research into novel and scalable copper oxidation nanostructuring techniques has alleviated some of this concern [4], however the robustness and durability after long hours of operation is unknown given the relatively harsh working environments encountered in industry.

## 10. Conclusions

A model framework of dropwise condensation heat transfer for micro/nanostructured superhydrophobic surfaces was developed. Unlike previous works, the current model is able to: 1) Predict the emergent droplet wetting morphology (PW jumping, PW non-jumping, or Wenzel) *via* coupling of the structure geometry and nucleation

density by considering local energy barriers to wetting; 2) Model non-constant contact angle droplet growth; and 3) Extend the previously developed droplet size distribution theory to both constant and non-constant contact angle droplets growing on surfaces experiencing coalescence-induced droplet jumping. The model was used to compute the overall surface heat transfer rate and study the effects of surface geometry and scale, nucleation density, and promoter coating. The results suggest the importance of emergent droplet wetting morphology on overall condensation heat flux. Specifically, distinct geometries existed which allowed for the formation of coalescence-induced jumping droplets having up to 110% overall surface heat flux enhancement over dropwise condensing geometries favoring W droplets, and 190% enhancement over flat hydrophobic surfaces. In addition, the results showed that scaling down the structure dimensions, while maintaining droplet coalescence at small length scales helps to sustain coalescence-induced droplet jumping over a larger range of geometries and maximize heat transfer performance enhancement.

Subsequently, the model was used to study the effects of four self-assembled monolayer promoter coatings on overall heat transfer, showing that surfaces exhibiting coalescence-induced droplet jumping are not sensitive to the intrinsic promoter coating wetting characteristics, which is in contrast to surfaces relying on gravity. Similarly, the impact of surface inclination with respect to gravity does not change the heat transfer characteristics of surfaces exhibiting jumping droplets, which is not the case for gravity based shedding surfaces, particularly at inclination angles in excess of 30°. The results indicate that structured surfaces may be the ideal pathway to achieving high heat flux dropwise condensation. This work provides guidelines for the rational design of structured superhydrophobic surfaces to maximize dropwise condensation heat transfer.

### **Acknowledgements**

The authors acknowledge the support from the MIT S3TEC Center, an Energy Frontier Research Center funded by the Department of Energy, Office of Science, Office of Basic Energy Sciences. R.E. acknowledges support from the Irish Research Council for Science, Engineering, and Technology, cofunded by Marie Curie Actions under FP7. This work was performed in part at the Center for Nanoscale Systems (CNS), a member of the National Nanotechnology Infrastructure Network (NNIN), which is supported by the National Science Foundation under NSF award number ECS-0335765. CNS is part of Harvard University.

## Nomenclature

$A$	Area of condensing surface [m <sup>2</sup> ]
$d$	Pillar diameter [m]
$E^*$	Wetting-state energy ratio [-]
$F_g$	Gravitational force acting on a droplet [N]
$F_\sigma$	Surface tension force acting on a droplet [N]
$g$	Gravitational acceleration, [9.81 N/kg]
$G$	Droplet growth rate [m/s]
$G_{pw}$	Partially wetting (variable contact angle) droplet growth rate [m/s]
$h$	Pillar height [m]
$h_{fg}$	Latent heat of vaporization [J/kg]
$h_i$	Liquid-vapor interface heat transfer coefficient [W/m <sup>2</sup> ·K]
$k_{HC}$	Hydrophobic promoter coating thermal conductivity [W/m·K]
$k_p$	Pillar/substrate thermal conductivity [W/m·K]
$k_w$	Water thermal conductivity [W/m·K]
$l$	Pillar center-to-center spacing [m]
$l_c$	Droplet coalescence length [m]
$\langle l_c \rangle$	Mean droplet coalescence length [m]
$\dot{m}$	Mass rate of condensate formation [kg/s]
$N$	Large droplet population density [m <sup>-3</sup> ]
$n$	Small droplet population density [m <sup>-3</sup> ]
$n_s$	Constant contact angle small droplet population density [m <sup>-3</sup> ]
$n_d$	Variable contact angle small droplet population density [m <sup>-3</sup> ]
$N_s$	Number of nucleation sites per unit area [m <sup>-2</sup> ]
$P$	Vapor saturation pressure [Pa]
$q$	Individual droplet heat transfer [W]
$q_{PW}$	Partially wetting morphology drop heat transfer [W]
$q_S$	Suspended morphology drop heat transfer [W]
$q_W$	Wenzel morphology drop heat transfer [W]
$q''$	Heat flux [W/m <sup>2</sup> ]
$q_{max}''$	Maximum structured surface heat flux [W/m <sup>2</sup> ]
$r$	Surface roughness [-]
$R$	Droplet radius [m]
$R_{min}$	Minimum droplet nucleation radius [m]
$R_{max}$	Droplet radius when variable contact angle growth ends (PW droplets) [m]
$\hat{R}$	Effective maximum droplet radius [m]
$R_e$	Droplet interaction radius [m]
$R_c$	Droplet curvature thermal resistance [K/W]
$R_{cd}$	Critical radius when $R_c = R_i$ [m]
$R_i$	Liquid-vapor interfacial thermal resistance [K/W]
$R_d$	Droplet conduction thermal resistance [K/W]
$R_{hc}$	Hydrophobic promoter coating thermal resistance [K/W]
$R_p$	Pillar structure thermal resistance [K/W]
$R_g$	Pinned liquid region thermal resistance [K/W]
$\bar{R}$	Gas constant [J/mol·K]
$S$	Droplet surface area removal rate due to large droplet sweeping [m <sup>2</sup> /s]
$t$	Time [s]
$\Delta T$	Surface subcooling temperature [K]
$\Delta T_c$	Droplet curvature temperature drop [K]
$\Delta T_{HC}$	Coating layer conduction temperature drop [K]
$\Delta T_i$	Liquid-vapor interfacial temperature drop [K]
$\Delta T_d$	Droplet body conduction temperature drop [K]
$\Delta T_{P,S}$	Suspended droplet pillar temperature drop [K]
$\Delta T_{P2}$	Pillar, coating and gap temperature drop [K]
$T_{b1}$	Liquid temperature at the droplet base [K]

$T_{b2}$	Temperature of pillar tops beneath coating [K]
$T_i$	Liquid-vapor interfacial temperature [K]
$T_{sat}$	Vapor saturation temperature [K]
$T_s$	Substrate/wall temperature [K]
$T_s'$	Substrate subcooled region temperature [K]
$V$	Volume [m <sup>3</sup> ]

#### Greek Symbols

$\alpha$	Condensation coefficient [-]
$\theta$	Contact angle [°]
$\theta_w$	Wenzel droplet contact angle [°]
$\theta_s$	Suspended droplet contact angle [°]
$\theta_{pw}$	Partially wetting droplet contact angle [°]
$\theta_a$	Advancing contact angle [°]
$\theta_r$	Receding contact angle [°]
$\Delta\theta$	Intrinsic contact angle hysteresis [°]
$\Theta$	Surface inclination angle from the vertical [°]
$\varphi$	Solid fraction [-]
$\sigma$	Surface tension [N/m]
$\rho_w$	Water density [kg/m <sup>3</sup> ]
$v_g$	Water vapor specific volume [m <sup>3</sup> /kg]
$\delta$	Thickness [m]
$\tau$	Sweeping period, [s]

#### Superscript

CB	Cassie-Baxter
PW	Partially wetting
S	Suspended
W	Wenzel
SAM	Self assembled monolayer

#### Subscripts

a	Advancing
c	Curvature, critical, coalescence
CB	Cassie Baxter
d	Droplet
e	Equilibrium, effective
F	Flat
g	Pinned liquid region under droplet
HC	Hydrophobic promoter coating
i	Liquid-vapor interface
p	Pillar
PW	Partially wetting
P-C-G	Pillar, coating, pinned liquid region
r	Receding
S	Suspended
w	Water
W	Wenzel

## References

- [1] Schmidt, E., Schurig, W., and Sellschopp, W., 1930, "Versuche über die Kondensation von Wasserdampf in Film- und Tropfenform," *Forsch. Ingenieurwes*, 1(2), pp. 53–63.
- [2] Miljkovic, N., Enright, R., and Wang, E. N., 2012, "Growth Dynamics During Dropwise Condensation on Nanostructured Superhydrophobic Surfaces," 3rd Micro/Nanoscale Heat & Mass Transfer International Conference, Atlanta, GA.
- [3] Ma, X. H., Rose, J. W., Xu, D. Q., Lin, J. F., and Wang, B. X., 2000, "Advances in dropwise condensation heat transfer: Chinese research," *Chem Eng J*, 78(2-3), pp. 87-93.
- [4] Enright, R., Dou, N., Miljkovic, N., Nam, Y., and Wang, E. N., 2012, "Condensation on Superhydrophobic Copper Oxide Nanostructures," 3rd Micro/Nanoscale Heat & Mass Transfer International Conference, Atlanta, GA.
- [5] Le Fevre, E. J., and Rose, J. W., 1964, "Heat-Transfer Measurements During Dropwise Condensation of Steam," *Int J Heat Mass Tran*, 7, pp. 272-273.
- [6] Welch, J., and Westwater, J. W., 1961, "Microscopic Study of Dropwise Condensation," *ASME International Developments in Heat Transfer*, 2, pp. 302-309.
- [7] Ma, X. H., Wang, S. F., Lan, Z., Peng, B. L., Ma, H. B., and Cheng, P., 2012, "Wetting Mode Evolution of Steam Dropwise Condensation on Superhydrophobic Surface in the Presence of Noncondensable Gas," *J Heat Trans-T Asme*, 134(2).
- [8] Glicksman, L. R., and Hunt, A. W., 1972, "Numerical Simulation of Dropwise Condensation," *Int J Heat Mass Tran*, 15(11), pp. 2251-2269.
- [9] Love, J. C., Estroff, L. A., Kriebel, J. K., Nuzzo, R. G., and Whitesides, G. M., 2005, "Self-Assembled Monolayers of Thiolates on Metals as a Form of Nanotechnology," *Chem Rev*, 105(4), pp. 1103-1169.
- [10] Andrews, H. G., Eccles, E. A., Schofield, W. C. E., and Badyal, J. P. S., 2011, "Three-Dimensional Hierarchical Structures for Fog Harvesting," *Langmuir*, 27(7), pp. 3798-3802.
- [11] Leach, R. N., Stevens, F., Langford, S. C., and Dickinson, J. T., 2006, "Dropwise Condensation: Experiments and Simulations of Nucleation and Growth of Water Drops in a Cooling System," *Langmuir*, 22(21), pp. 8864-8872.
- [12] Boreyko, J. B., and Chen, C. H., 2009, "Self-Propelled Dropwise Condensate on Superhydrophobic Surfaces," *Phys Rev Lett*, 103(18), pp. 184501-184501 - 184501-184504.
- [13] Lafuma, A., and Quere, D., 2003, "Superhydrophobic States," *Nature Materials*, 2(7), pp. 457-460.
- [14] Dietz, C., Rykaczewski, K., Fedorov, A. G., and Joshi, Y., 2010, "Visualization of Droplet Departure on a Superhydrophobic Surface and Implications to Heat Transfer Enhancement During Dropwise Condensation," *Appl Phys Lett*, 97(3), pp. 033104-033101 - 033104-033103.
- [15] Graham, C., and Griffith, P., 1973, "Drop Size Distributions and Heat-Transfer in Dropwise Condensation," *Int J Heat Mass Tran*, 16(2), pp. 337-346.
- [16] Rose, J. W., 1967, "On the Mechanism of Dropwise Condensation," *Int J Heat Mass Tran*, 10, pp. 755-762.
- [17] Anderson, D. M., Gupta, M. K., Voevodin, A. A., Hunter, C. N., Putnam, S. A., Tsukruk, V. V., and Fedorov, A. G., 2012, "Using Amphiphilic Nanostructures To Enable Long-Range Ensemble Coalescence and Surface Rejuvenation in Dropwise Condensation," *Acs Nano*, 6(4), pp. 3262-3268.
- [18] Boreyko, J. B., Zhao, Y. J., and Chen, C. H., 2011, "Planar jumping-drop thermal diodes," *Appl Phys Lett*, 99(23).
- [19] Dietz, C., Rykaczewski, K., Fedorov, A., and Joshi, Y., 2010, "ESEM Imaging of Condensation on a Nanostructured Superhydrophobic Surface," *J Heat Trans-T Asme*, 132(8), pp. 080904-080901.
- [20] Narhe, R. D., and Beysens, D. A., 2006, "Water Condensation on a Super-Hydrophobic Spike Surface," *Europhys Lett*, 75(1), pp. 98-104.
- [21] Varanasi, K. K., Hsu, M., Bhate, N., Yang, W. S., and Deng, T., 2009, "Spatial Control in the Heterogeneous Nucleation of Water," *Appl Phys Lett*, 95(9), pp. 094101-094101 - 094101-094103.
- [22] Enright, R., Miljkovic, N., Al-Obeidi, A., Thompson, C. V., and Wang, E. N., 2012, "Superhydrophobic Condensation: The Role of Length Scale and Energy Barriers.," *Langmuir*, Accepted.
- [23] Miljkovic, N., Enright, R., Maroo, S. C., Cho, H. J., and Wang, E. N., 2011, "Liquid Evaporation on Superhydrophobic and Superhydrophilic Nanostructured Surfaces," *J Heat Transf*, 133(8), pp. 080903-080901.
- [24] Miljkovic, N., Enright, R., and Wang, E. N., 2012, "Effect of Droplet Morphology on Growth Dynamics and Heat Transfer during Condensation on Superhydrophobic Nanostructured Surfaces," *Acs Nano*, 6(2), pp. 1776–1785.
- [25] Le Fevre, E. J., and Rose, J. W., 1966, "A Theory of Heat Transfer by Dropwise Condensation," *Proceedings of the Third International Heat Transfer Conference*, 2, pp. 362-375.

- [26] Rose, J. W., and Glicksman, L. R., 1973, "Dropwise condensation - the distribution of drop sizes," *Int J Heat Mass Tran*, 16, pp. 411-425.
- [27] Tanaka, H., and Tsuruta, T., 1984, "A Microscopic Study of Dropwise Condensation," *Int J Heat Mass Tran*, 27(3), pp. 327-335.
- [28] AbuOrabi, M., 1998, "Modeling of Heat Transfer in Dropwise Condensation," *Int J Heat Mass Tran*, 41(1), pp. 81-87.
- [29] Kim, S., and Kim, K. J., 2011, "Dropwise Condensation Modeling Suitable for Superhydrophobic Surfaces," *J Heat Transf*, 133(8), pp. 081502-081501 - 081502-081507.
- [30] Cassie, A. B. D., and Baxter, S., 1944, "Wettability of Porous Surfaces " *Trans. Faraday Soc*, 40 pp. 546-551.
- [31] Wenzel, R. N., 1936, "Resistance of Solid Surfaces to Wetting by Water," *Ind. Eng. Chem.*, 28, pp. 988-994.
- [32] Rykaczewski, K., and Scott, J. H. J., 2011, "Methodology for Imaging Nano-to-Microscale Water Condensation Dynamics on Complex Nanostructures," *Acs Nano*, 5(7), pp. 5962-5968.
- [33] Rykaczewski, K., Scott, J. H. J., Rajauria, S., Chinn, J., Chinn, A. M., and Jones, W., 2011, "Three Dimensional Aspects of Droplet Coalescence During Dropwise Condensation on Superhydrophobic Surfaces," *Soft Matter*, 7(19), pp. 8749-8752.
- [34] Das, A. K., Kilty, H. P., Marto, P. J., Andeen, G. B., and Kumar, A., 2000, "The use of an organic self-assembled monolayer coating to promote dropwise condensation of steam on horizontal tubes," *J Heat Trans-T Asme*, 122(2), pp. 278-286.
- [35] Vemuri, S., Kim, K. J., Wood, B. D., Govindaraju, S., and Bell, T. W., 2006, "Long term testing for dropwise condensation using self-assembled monolayer coatings of n-octadecyl mercaptan," *Appl Therm Eng*, 26(4), pp. 421-429.
- [36] Choi, W., Tuteja, A., Mabry, J. M., Cohen, R. E., and McKinley, G. H., 2009, "A modified Cassie-Baxter relationship to explain contact angle hysteresis and anisotropy on non-wetting textured surfaces," *J Colloid Interf Sci*, 339(1), pp. 208-216.
- [37] Anand, S., and Son, S. Y., 2010, "Sub-Micrometer Dropwise Condensation Under Superheated and Rarefied Vapor Condition," *Langmuir*, 26(22), pp. 17100-17110.
- [38] Rykaczewski, K., Scott, J. H. J., and Fedorov, A. G., 2011, "Electron Beam Heating Effects During Environmental Scanning Electron Microscopy Imaging of Water Condensation on Superhydrophobic Surfaces," *Appl Phys Lett*, 98(9), pp. 093106-093101 - 093106-093103.
- [39] Kaschiev, D., 2000, *Nucleation: Basic Theory With Applications*, Butterworth Heinemann, Oxford.
- [40] Tam, D., von Arnim, V., McKinley, G. H., and Hosoi, A. E., 2009, "Marangoni Convection in Droplets on Superhydrophobic Surfaces," *J Fluid Mech*, 624, pp. 101-123.
- [41] Carey, V. P., 2008, *Liquid-Vapor Phase-Change Phenomena: An Introduction to the Thermophysics of Vaporization and Condensation Processes in Heat Transfer Equipment*, Taylor and Francis, New York.
- [42] Schrage, R. W., 1953, "A Theoretical Study of Interphase Mass Transfer," Thesis, Columbia University., New York,.
- [43] Umur, A., and Griffith, P., 1965, "Mechanism of Dropwise Condensation," *J Heat Transf*, 87(2), pp. 275-282.
- [44] Dimitrakopoulos, P., and Higdon, J. J. L., 1999, "On The Gravitational Displacement of Three-Dimensional Fluid Droplets From Inclined Solid Surfaces," *J Fluid Mech*, 395, pp. 181-209.
- [45] Kim, H. Y., Lee, H. J., and Kang, B. H., 2002, "Sliding of Liquid Drops Down an Inclined Solid Surface," *J Colloid Interf Sci*, 247(2), pp. 372-380.
- [46] Raj, R., Enright, R., Zhu, Y., Adera, S., and Wang, E. N., 2012, "A Unified Model for Contact Angle Hysteresis on Heterogeneous and Superhydrophobic Surfaces," *Langmuir*, Submitted.
- [47] Chen, C. H., Cai, Q. J., Tsai, C. L., Chen, C. L., Xiong, G. Y., Yu, Y., and Ren, Z. F., 2007, "Dropwise Condensation on Superhydrophobic Surfaces With Two-Tier Roughness," *Appl Phys Lett*, 90(17), pp. 173108-173101 - 173108-173103.
- [48] Lau, K. K. S., Bico, J., Teo, K. B. K., Chhowalla, M., Amaratunga, G. A. J., Milne, W. I., McKinley, G. H., and Gleason, K. K., 2003, "Superhydrophobic Carbon Nanotube Forests," *Nano Lett*, 3(12), pp. 1701-1705.
- [49] Rykaczewski, K., 2012, "Microdroplet Growth Mechanism during Water Condensation on Superhydrophobic Surfaces," *Langmuir*, 28(20), pp. 7720-7729.
- [50] Rykaczewski, K., Osborn, W. A., Chinn, J., Walker, M. L., Scott, J. H. J., Jones, W., Hao, C., Yao, S., and Wang, Z., 2012, "How nanorough is rough enough to make a surface superhydrophobic during water condensation?," *Soft Matter*, 8, pp. 8786-8794.
- [51] Rose, J. W., 2002, "Dropwise condensation theory and experiment: a review," *P I Mech Eng a-J Pow*, 216(A2), pp. 115-128.



- [52] Woodruff, D. W., and Westwater, J. W., 1981, "Steam Condensation on Various Gold Surfaces," *J Heat Trans-T Asme*, 103(4), pp. 685-692.
- [53] Wilkins, D. G., Bromley, L. A., and Read, S. M., 1973, "Dropwise and Filmwise Condensation of Water Vapor on Gold," *Aiche J*, 19(1), pp. 119-123.
- [54] Chen, X., Wu, J., Ma, R., Hua, M., Koratkar, N., Yao, S., and Wang, Z., 2011, "Nanograsped Micropyramidal Architectures for Continuous Dropwise Condensation," *Adv Funct Mater*, 21, pp. 4617–4623.
- [55] Miljkovic, N., Enright, R., and Wang, E. N., 2012, "Liquid Freezing Dynamics on Hydrophobic and Superhydrophobic Surfaces," *J Heat Trans-T Asme*, 134(8).
- [56] Miljkovic, N., and Wang, E. N., 2011, "Modeling and optimization of hybrid solar thermoelectric systems with thermosyphons," *Sol Energy*, 85(11), pp. 2843-2855.
- [57] McCarthy, M., Peters, T., Allison, J., Espinosa, A., Jenicek, D., Kariya, A., Koveal, C., Brisson, J. G., Lang, J. H., and Wang, E. N., 2010, "Design and Analysis of High-Performance Air-Cooled Heat Exchanger with an Integrated Capillary-Pumped Loop Heat Pipe," *Intersoc C Thermal T*.

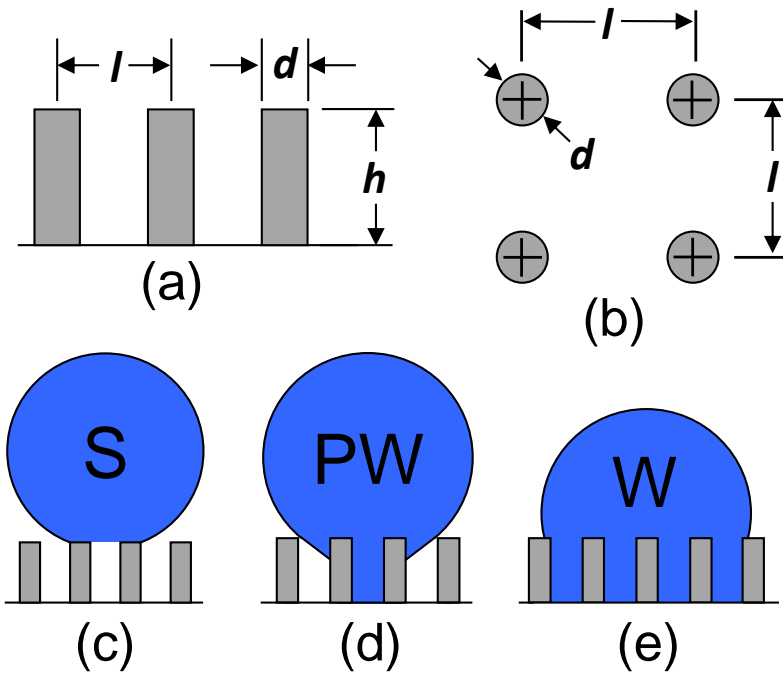


**Figure 1** – Schematics of the modeled structured surface showing (a) side view and (b) top view of the characteristic structure dimensions  $h$ ,  $d$ , and  $l$  representing the pillar height, diameter and center-to-center spacing, respectively. Schematics showing the (c) suspended (S), (d) partially wetting (PW), and (e) Wenzel (W) morphologies.

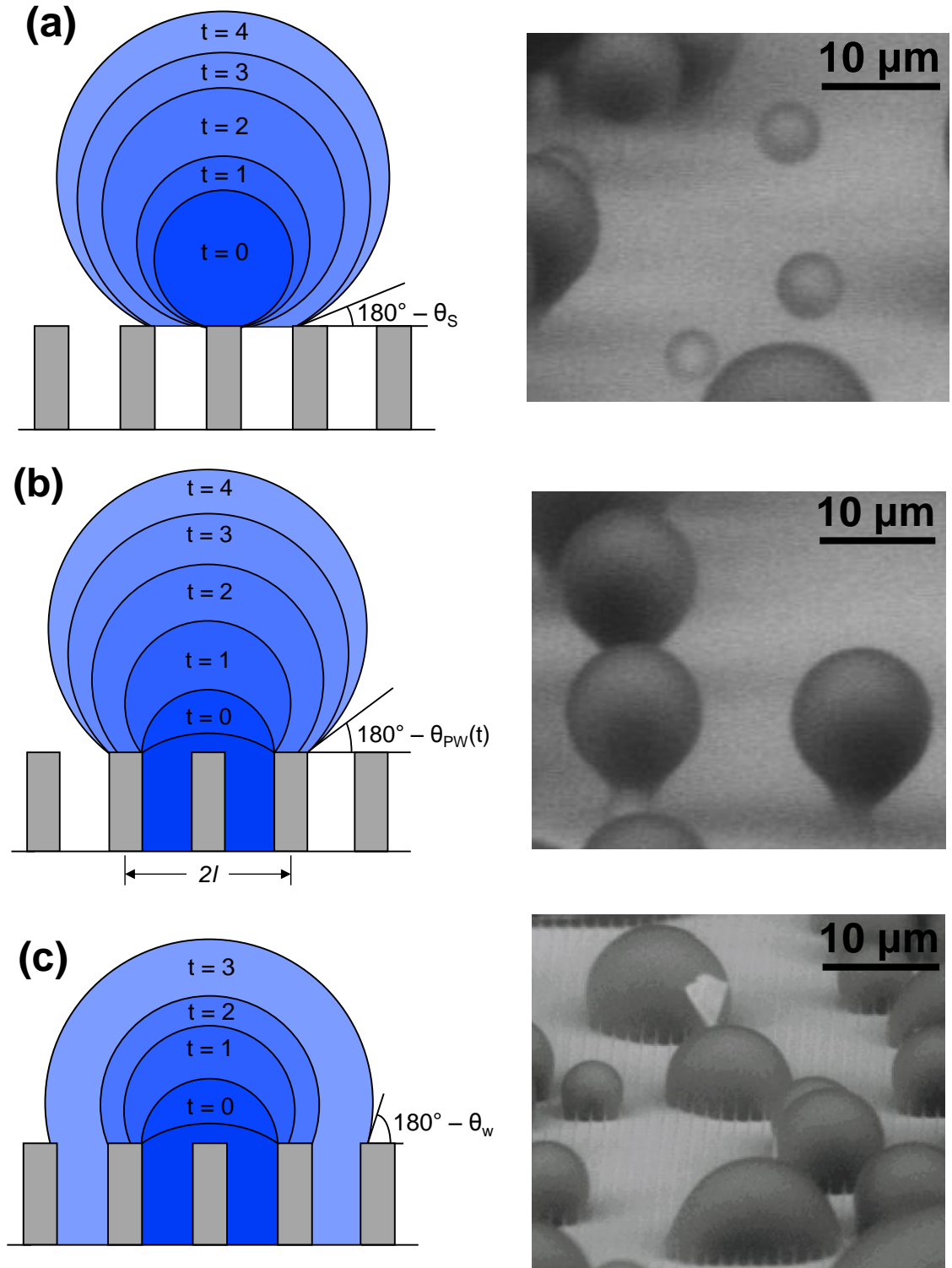


**Figure 2** – Time-lapse schematics of (a) S, (b) PW, and (c) W droplet morphologies during growth on the structured surface. To the right of the schematics are corresponding environmental scanning electron microscopy (ESEM) images of droplets with the different morphologies on a nanostructured surface ( $h = 6.1 \mu\text{m}$ ,  $l = 2 \mu\text{m}$ ,  $d = 300 \text{ nm}$ ) [23, 24]. Schematics not to scale.

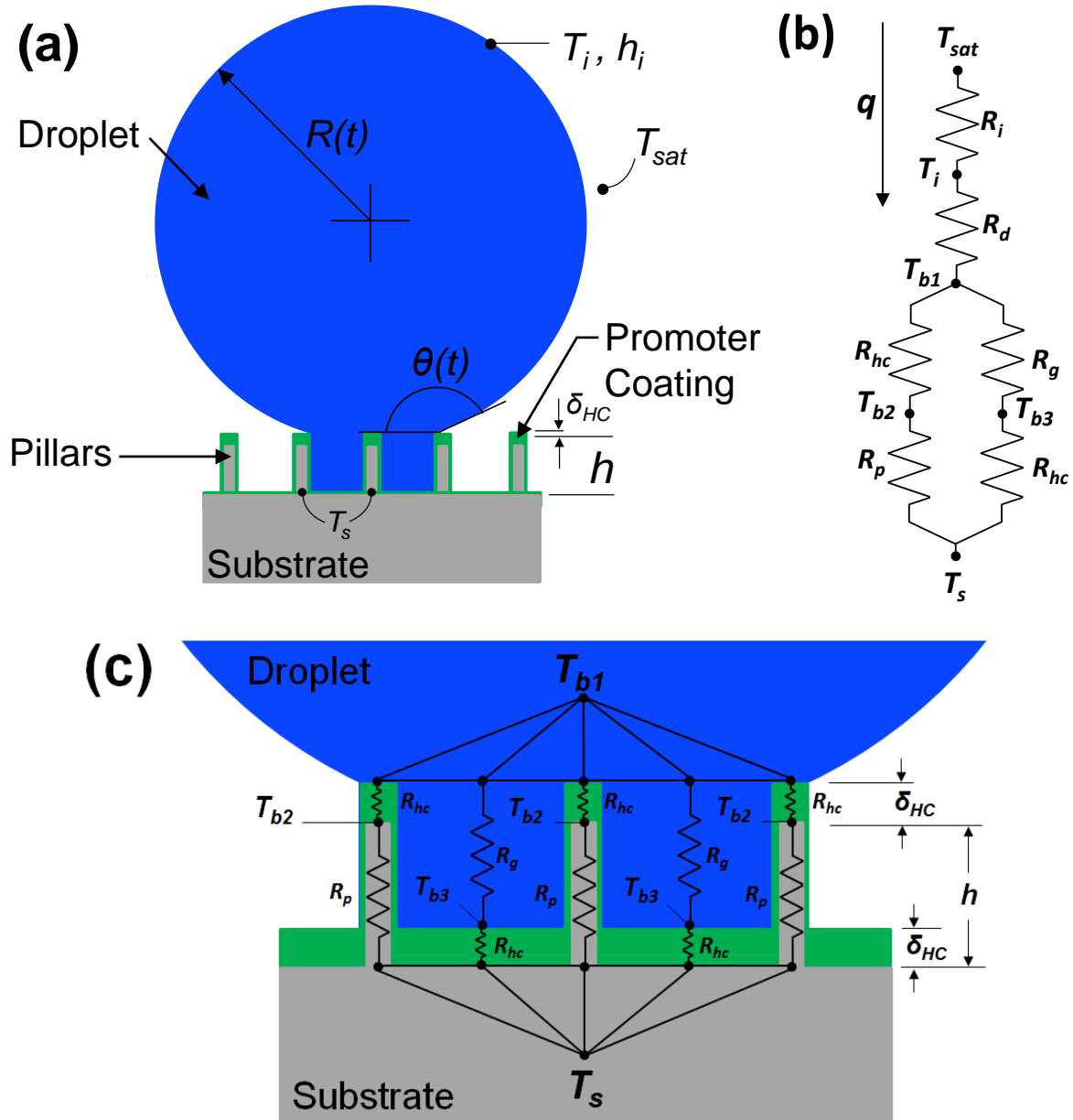


**Figure 3** – (a) Schematic of the droplet on the condensing surface growing in the PW morphology. (b) Droplet thermal resistance diagram showing the liquid-vapor interface ( $R_i$ ), droplet conduction ( $R_d$ ), hydrophobic promoter coating ( $R_{hc}$ ), pillar ( $R_p$ ), and gap ( $R_g$ ) thermal resistances. (c) Thermal resistance network in the droplet and pillar structure. The schematic shows the parallel path of heat flowing through i) the coating ( $R_{HC}$ ) followed by the pillar ( $R_p$ ) and ii) the liquid bridge ( $R_g$ ) followed by the coating ( $R_{HC}$ ). Schematics not to scale.

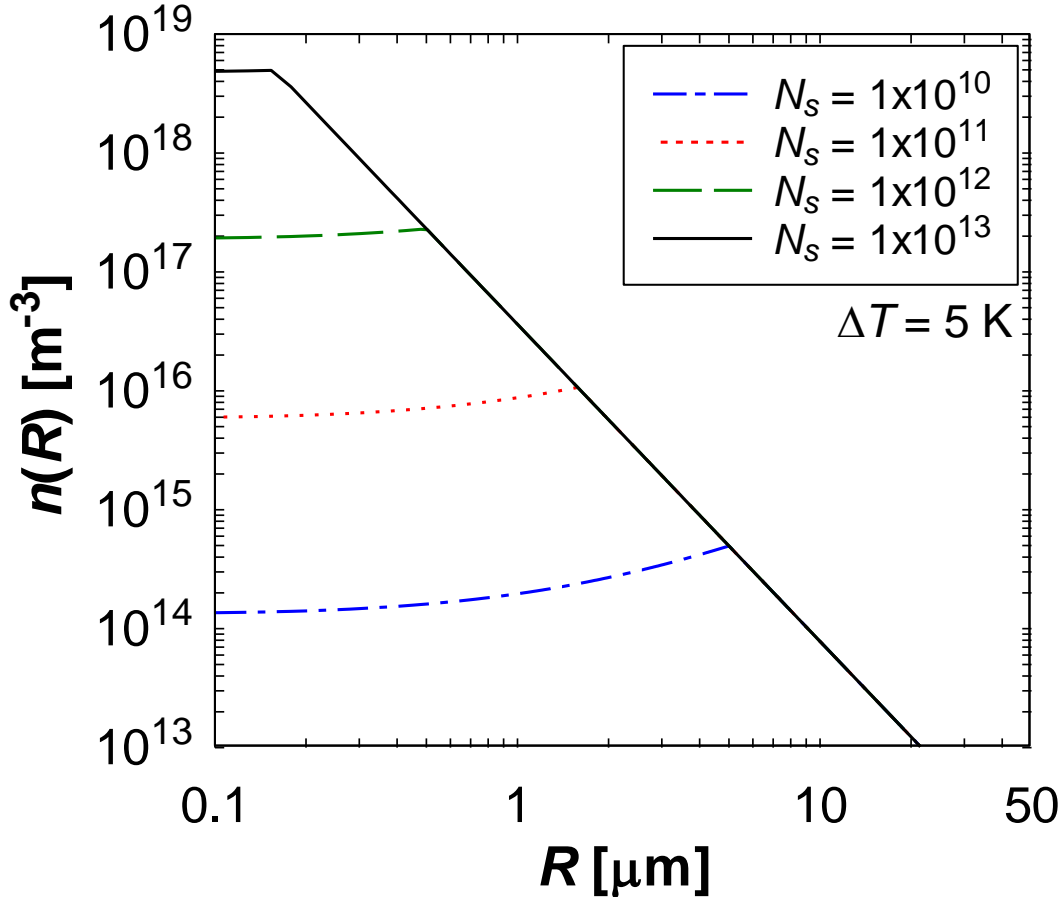


**Figure 4** – Droplet size distribution for a surface with droplet removal by gravity (flat hydrophobic surfaces) as a function of droplet radius  $R$  for various nucleation densities  $N_s$ . The population density is shown for small droplets ( $n(R)$ ) with color curves and large coalescing droplets ( $N(R)$ ) with the black curve. Higher nucleation densities lead to earlier droplet coalescence and smaller coalescence lengths ( $l_c = 2R_c$ ). The population of small ( $R < R_c$ ) non-interacting droplets is larger than large ( $R > R_c$ ) droplets because large droplets experience coalescence in addition to being swept off the surface. Model parameters:  $h = 10 \mu\text{m}$ ,  $l = 4 \mu\text{m}$ ,  $d = 300 \text{ nm}$ ,  $\Delta T = T_{\text{sat}} - T_s = 5 \text{ K}$ ,  $\theta_a/\theta_r = 121.6^\circ/86.1^\circ$ .

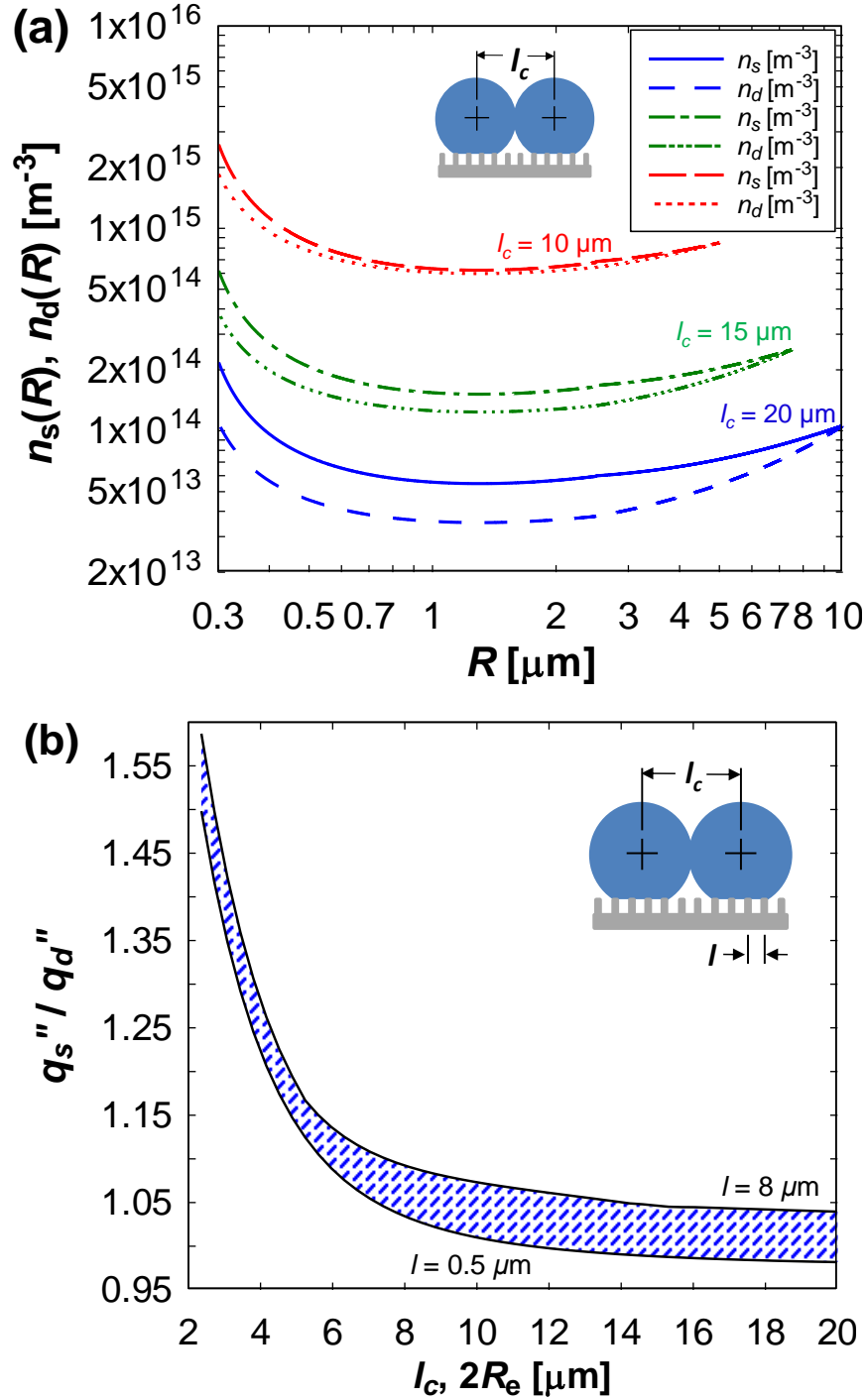


**Figure 5** – (a) Droplet population densities for surfaces exhibiting coalescence induced droplet removal as a function of radius  $R$  for a variety of nucleation densities  $N_S$  with constant contact angle  $n_s(R)$  (solid lines) and variable contact angle  $n_d(R)$  (dotted lines). Higher nucleation densities result in earlier droplet coalescence and smaller coalescence lengths ( $l_c = 2R_e$ ). Inset: schematic showing coalescence length ( $l_c$ ). (b) Ratio of the ‘dynamic’ surface heat flux  $q_d''$  (Eq. (47)) to the static surface heat flux  $q_s''$  (Eq. (46)) as a function of droplet coalescence length ( $l_c$ ) and structured surface pillar-to-pillar spacing ( $l$ ). The shaded includes the results for the different pillar spacings ( $0.5 \mu\text{m} < l < 8 \mu\text{m}$ ). The static contact angle droplet model over predicts the surface heat flux at small departure sizes, which shows the importance of using the dynamic contact model for predicting PW droplet performance. Model parameters:  $h = 10 \mu\text{m}$ ,  $l = 4 \mu\text{m}$ ,  $d = 300 \text{ nm}$ ,  $\Delta T = 5 \text{ K}$ ,  $\theta_a/\theta_r = 121.6^\circ/86.1^\circ$ .

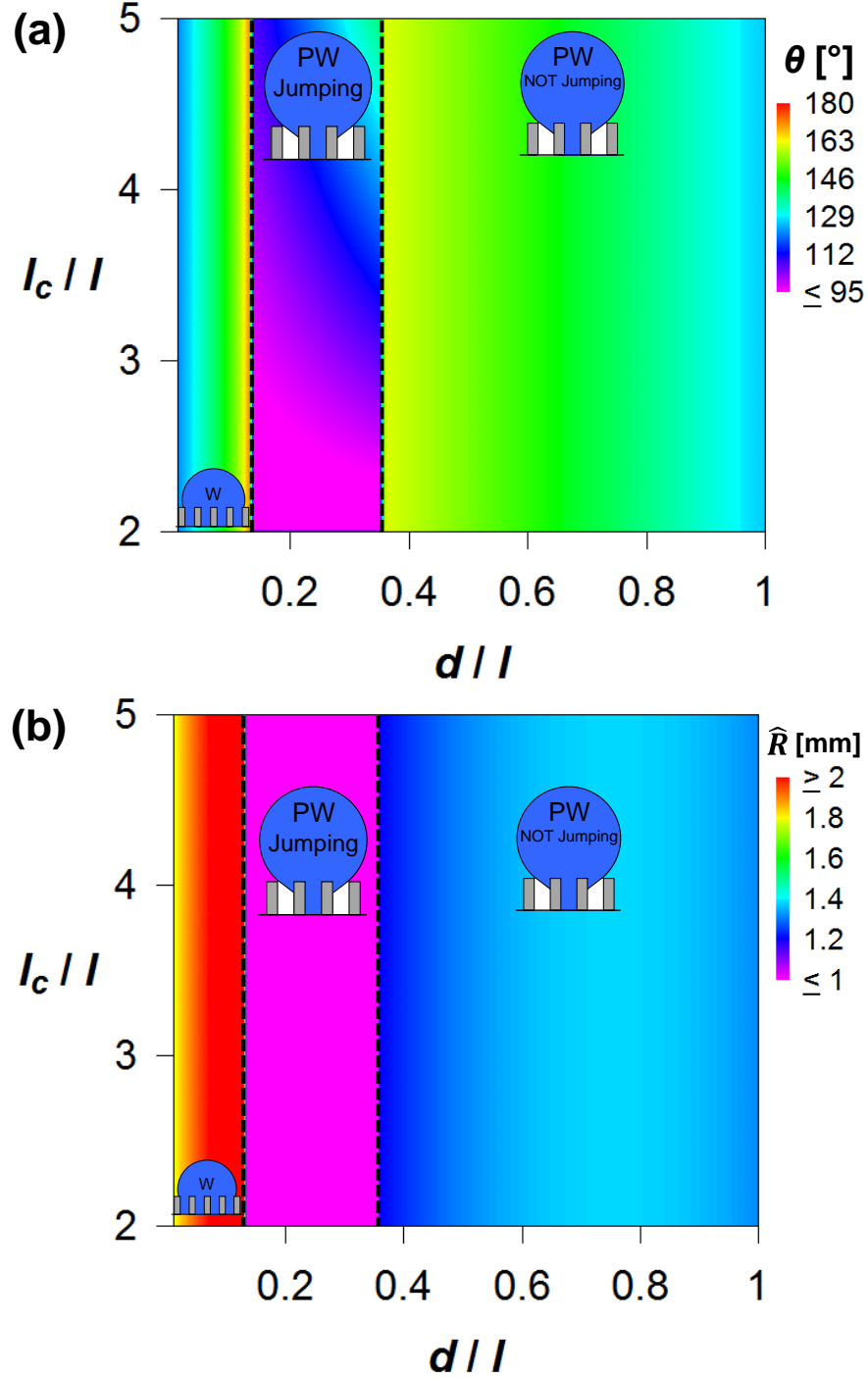


**Figure 6** – (a) Condensing droplet apparent contact angle  $\theta$  as a function of coalescence length ( $l_c/l$ ) and ratio of pillar diameter to center-to-center spacing ( $d/l$ ). Distinct regions of differing droplet wetting morphologies exist based on the wetting criteria (Section 2). For  $d/l > 0.36$ , the PW droplet morphology is favored, however droplet jumping is not possible due to the high solid fraction ( $\phi > 0.1$ ) and high contact line pinning to the surface structure. For  $l_c/l < 2$  (not-shown), liquid films and pinned W droplets are formed due to droplet merging within the unit cell of the structure. (b) Condensing droplet departure radius,  $\hat{R}$  as a function of coalescence length ( $l_c/l$ ) and ratio of pillar diameter to center-to-center spacing ( $d/l$ ). Regimes of W droplet formation have higher departure radii than PW droplets due to higher surface adhesion and contact angle hysteresis. Model parameters:  $h = 10 \mu\text{m}$ ,  $l = 4 \mu\text{m}$ ,  $d = 300 \text{ nm}$ ,  $\Delta T = 5 \text{ K}$ ,  $\theta_a/\theta_r = 121.6^\circ/86.1^\circ$ ,  $k_{\text{HC}} \approx 0.2 \text{ W/mK}$  [28],  $k_p = 150 \text{ W/mK}$ ,  $\delta_{\text{HC}} = 1 \text{ nm}$ . Insets: emergent droplet morphology schematics for each region.

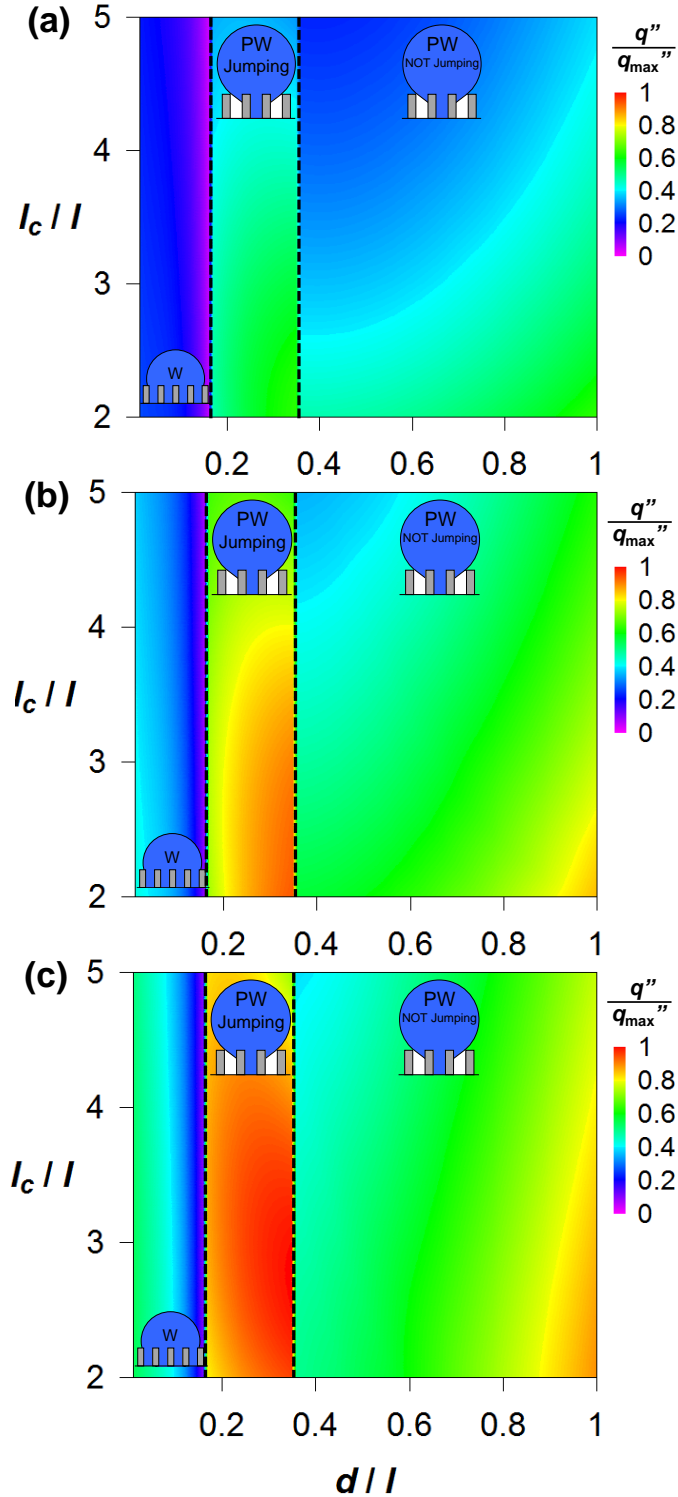


**Figure 7** – Normalized overall steady-state surface heat flux  $q''/q''_{\max}$ , as a function of coalescence length ( $l_c/l$ ) and ratio of pillar diameter to center-to-center spacing ( $d/l$ ) for (a)  $h = 5 \mu\text{m}$ , (b)  $h = 2 \mu\text{m}$ , and (c)  $h = 1 \mu\text{m}$ . Scaling down the surface structure ((a) to (c)) enhances performance due to the reduced micro/nanostructure thermal resistance. Regions favoring PW jumping droplet removal show peak heat fluxes for all three cases ((a) to (c)).  $q''_{\max}$  was determined from examining the peak heat flux in all three cases, which occurred for the smallest scale structure (c),  $q''_{\max} = 342.12 \text{ kW/m}^2$ . Model parameters:  $h/l = 2$ ,  $\Delta T = 5 \text{ K}$ ,  $\theta_a/\theta_r = 121.6^\circ/86.1^\circ$ ,  $k_{\text{HC}} = 0.2 \text{ W/mK}$ ,  $k_p = 150 \text{ W/mK}$ ,  $\delta_{\text{HC}} = 1 \text{ nm}$ . Insets: emergent droplet morphology schematics for each region.



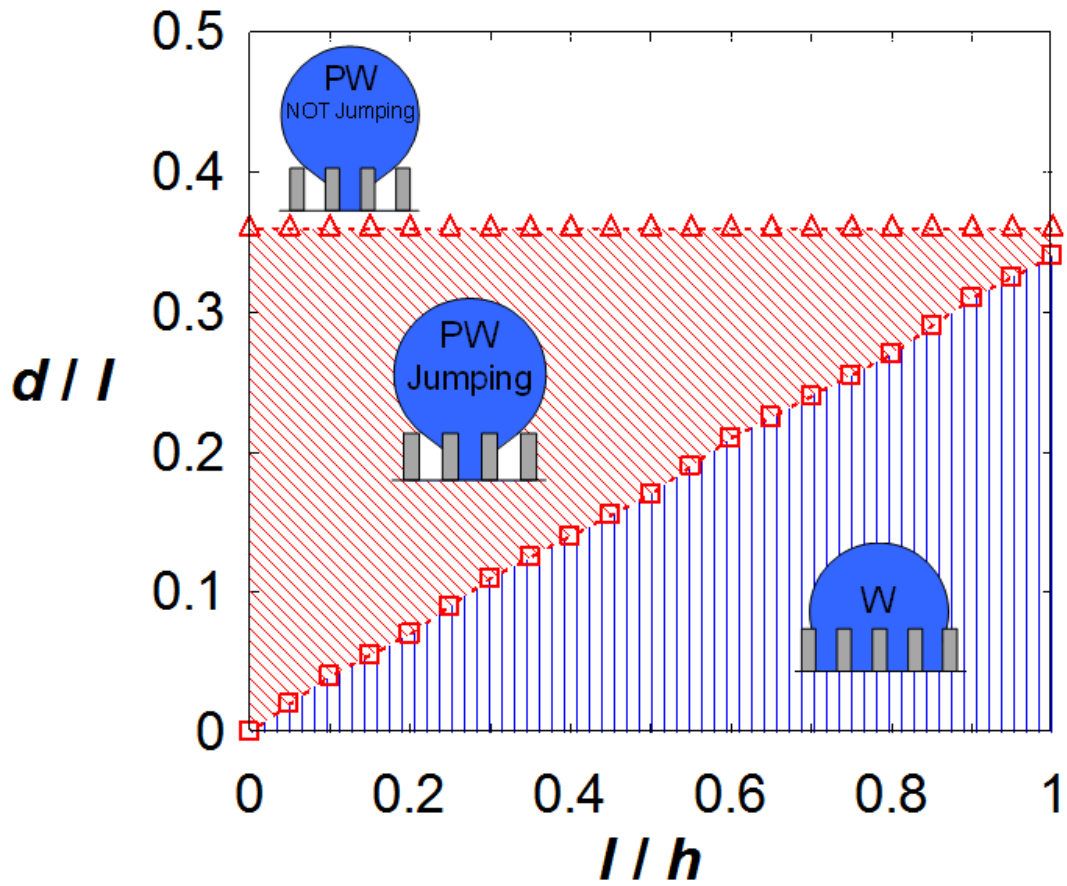


**Figure 8** – Structured surface steady-state wetting morphology as a function of the pillar diameter to center-to-center spacing ratio ( $d/l$ ) and the center-to-center spacing to pillar height ratio ( $l/h$ ). Scaling down the surface structure ( $l/h$ ) broadens the  $d/l$  regime where PW jumping droplets are observed. Insets: emergent droplet morphology schematics for each region.

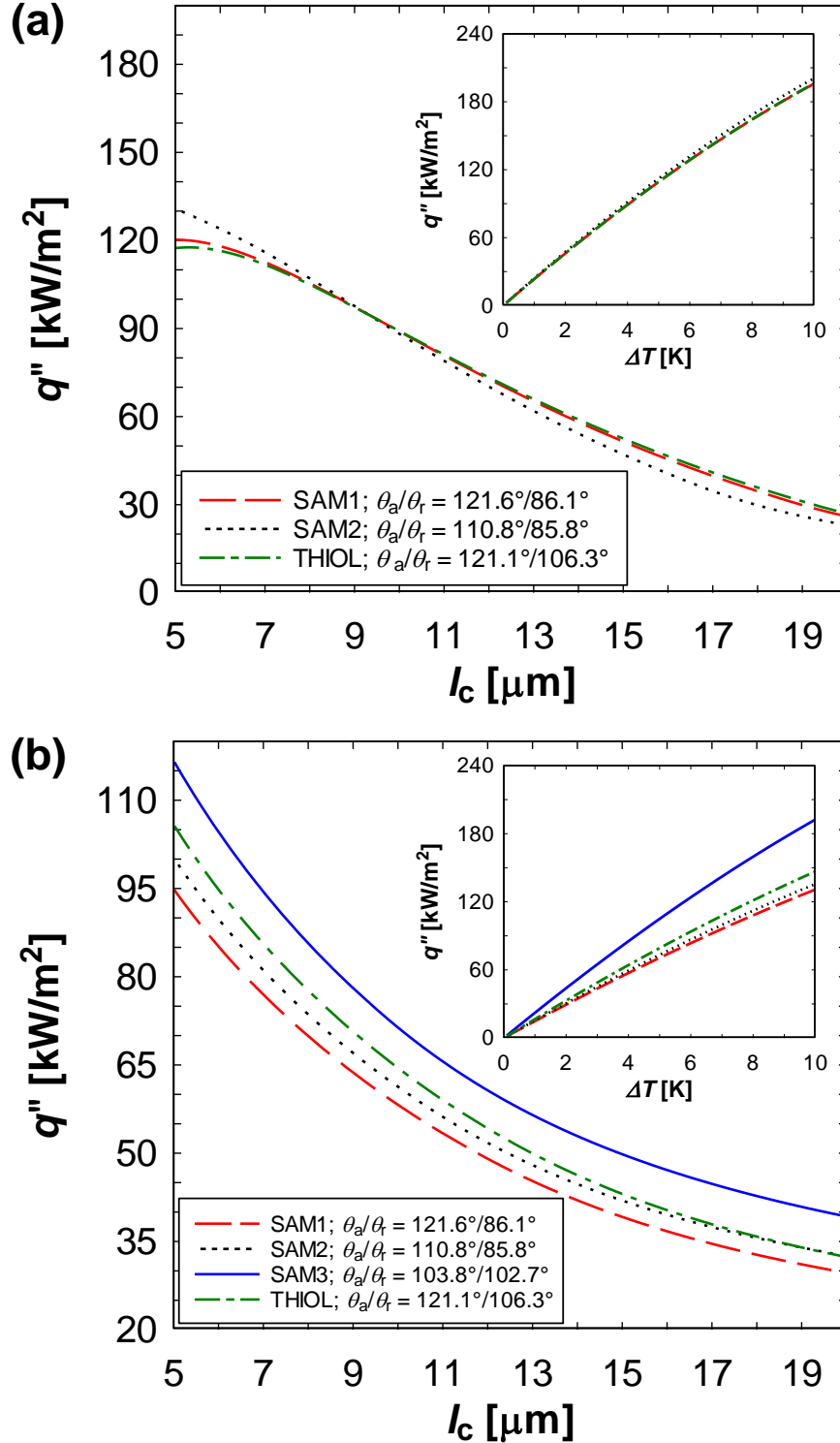


**Figure 9** –Structured surface steady-state heat flux  $q''$  as a function of coalescence length  $l_c$  for four different promoter coatings with (a) coalescence-induced droplet jumping (no sweeping) and (b) gravitational droplet removal (sweeping). The surface heat flux is not sensitive to the promoter coating for surfaces with coalescence-induced droplet departure. Heat flux ( $q''$ ) is highly dependent on the promoter coating for surfaces relying on gravity for droplet removal due to the strong dependence of droplet/surface adhesion on contact angle hysteresis. Insets: Surface heat flux ( $q''$ ) as a function of temperature difference ( $\Delta T = T_{\text{sat}} - T_s$ ) for the four different promoter coatings and model parameters:  $h = 5 \mu\text{m}$ ,  $l = 2.5 \mu\text{m}$ ,  $\Delta T = 5\text{K}$ ,  $l_c = 7.5 \mu\text{m}$ ,  $k_{\text{HC}} = 0.2 \text{ W/mK}$ ,  $k_p = 150 \text{ W/mK}$ ,  $\delta_{\text{HC}} = 1 \text{ nm}$ .

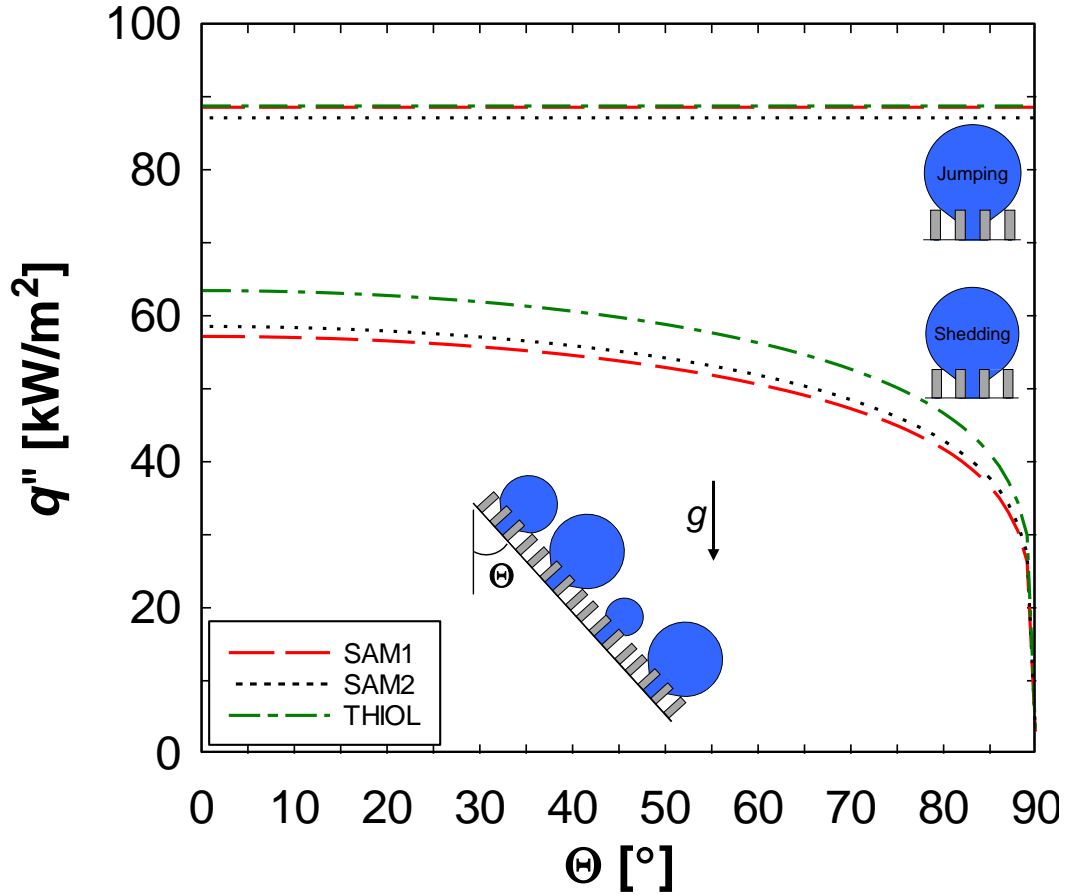


**Figure 10** – Structured surface steady-state heat flux  $q''$  as a function of the surface inclination angle  $\Theta$  for SAM coated (SAM1, SAM2, and THIOL) structured surfaces exhibiting coalescence-induced droplet jumping ( $d/l = 0.3$ ) and gravity based droplet shedding ( $d/l = 0.4$ ). Jumping surfaces showed little sensitivity to the orientation owing to their ability to shed droplets at length scales well below the capillary length ( $\hat{R} \ll 1$  mm). Surfaces exhibiting gravity based shedding showed a strong dependence on  $\Theta$ , due to the  $\cos\Theta$  dependence of the gravitational body force acting on the condensing droplets needed to overcome the surface tension force (Eq. (25)). Inset: condensing surface orientation schematic. Model parameters:  $h = 5 \mu\text{m}$ ,  $l = 2.5 \mu\text{m}$ ,  $\Delta T = 5 \text{ K}$ ,  $l_c = 10 \mu\text{m}$ ,  $k_{\text{HC}} = 0.2 \text{ W/mK}$ ,  $k_p = 150 \text{ W/mK}$ ,  $\delta_{\text{HC}} = 1 \text{ nm}$ .

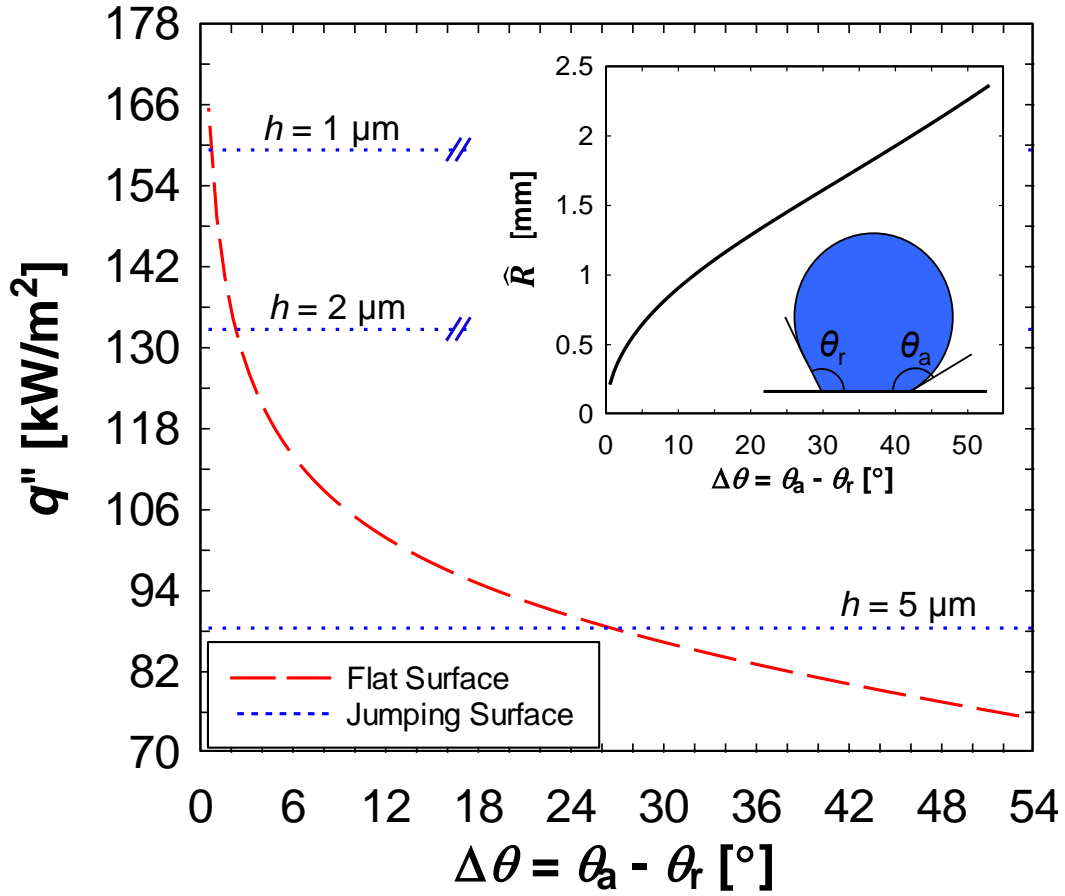


**Figure 11** –Structured (jumping) and flat (gravity shedding) surface steady-state heat flux  $q''$  as a function of intrinsic promoter coating contact angle hysteresis  $\Delta\theta$  for three structured surfaces coated with the SAM1 promoter.

As  $\Delta\theta$  decreases for the flat surface,  $q''$  increases due to the lower droplet adhesion to the surface and lower departure radii (Inset). As a result, the flat surfaces begin to show enhanced  $q''$  compared to the structured surfaces.

Inset: Droplet departure diameter ( $\hat{R}$ ), as a function of intrinsic flat surface contact angle hysteresis ( $\Delta\theta$ ). Model parameters:  $\Delta T = 5$  K,  $l_c = 10 \mu\text{m}$ ,  $k_{\text{HC}} = 0.2$  W/mK,  $k_p = 150$  W/mK,  $\delta_{\text{HC}} = 1$  nm, SAM1 coating:

$$\theta_a/\theta_r = 121.6^\circ/86.1^\circ.$$

## Caption List:

**Figure 1** – Schematics of the modeled structured surface showing (a) side view and (b) top view of the characteristic structure dimensions  $h$ ,  $d$ , and  $l$  representing the pillar height, diameter and center-to-center spacing, respectively. Schematics showing the (c) suspended (S), (d) partially wetting (PW), and (e) Wenzel (W) morphologies.

**Figure 2** – Time-lapse schematics of (a) S, (b) PW, and (c) W droplet morphologies during growth on the structured surface. To the right of the schematics are corresponding environmental scanning electron microscopy (ESEM) images of droplets with the different morphologies on a nanostructured surface ( $h = 6.1 \mu\text{m}$ ,  $l = 2 \mu\text{m}$ ,  $d = 300 \text{ nm}$ ) [23, 24]. Schematics not to scale.

**Figure 3** – (a) Schematic of the droplet on the condensing surface growing in the PW morphology. (b) Droplet thermal resistance diagram showing the liquid-vapor interface ( $R_i$ ), droplet conduction ( $R_d$ ), hydrophobic promoter coating ( $R_{hc}$ ), pillar ( $R_p$ ), and gap ( $R_g$ ) thermal resistances. (c) Thermal resistance network in the droplet and pillar structure. The schematic shows the parallel path of heat flowing through i) the coating ( $R_{HC}$ ) followed by the pillar ( $R_p$ ) and ii) the liquid bridge ( $R_b$ ) followed by the coating ( $R_{HC}$ ). Schematics not to scale.

**Figure 4** – Droplet size distribution for a surface with droplet removal by gravity (flat hydrophobic surfaces) as a function of droplet radius  $R$  for various nucleation densities  $N_s$ . The population density is shown for small droplets ( $n(R)$ ) with color curves and large coalescing droplets ( $N(R)$ ) with the black curve. Higher nucleation densities lead to earlier droplet coalescence and smaller coalescence lengths ( $l_c = 2R_c$ ). The population of small ( $R < R_c$ ) non-interacting droplets is larger than large ( $R > R_c$ ) droplets because large droplets experience coalescence in addition to being swept off the surface. Model parameters:  $h = 10 \mu\text{m}$ ,  $l = 4 \mu\text{m}$ ,  $d = 300 \text{ nm}$ ,  $\Delta T = T_{\text{sat}} - T_s = 5 \text{ K}$ ,  $\theta_a/\theta_r = 121.6^\circ/86.1^\circ$ .

**Figure 5** – (a) Droplet population densities for surfaces exhibiting coalescence induced droplet removal as a function of radius  $R$  for a variety of nucleation densities  $N_s$  with constant contact angle  $n_s(R)$  (solid lines) and variable contact angle  $n_d(R)$  (dotted lines). Higher nucleation densities result in earlier droplet coalescence and smaller coalescence lengths ( $l_c = 2R_c$ ). Inset: schematic showing coalescence length ( $l_c$ ). (b) Ratio of the ‘dynamic’ surface heat flux  $q_d''$  (Eq. (47)) to the static surface heat flux  $q_s''$  (Eq. (46)) as a function of droplet coalescence length ( $l_c$ ) and structured surface pillar-to-pillar spacing ( $l$ ). The shaded includes the results for the different pillar spacings ( $0.5 \mu\text{m} < l < 8 \mu\text{m}$ ). The static contact angle droplet model over predicts the surface heat flux at small departure sizes, which shows the importance of using the dynamic contact model for predicting PW droplet performance. Model parameters:  $h = 10 \mu\text{m}$ ,  $l = 4 \mu\text{m}$ ,  $d = 300 \text{ nm}$ ,  $\Delta T = 5 \text{ K}$ ,  $\theta_a/\theta_r = 121.6^\circ/86.1^\circ$ .

**Figure 6** – (a) Condensing droplet apparent contact angle  $\theta$  as a function of coalescence length ( $l_c/l$ ) and ratio of pillar diameter to center-to-center spacing ( $d/l$ ). Distinct regions of differing droplet wetting morphologies exist based on the wetting criteria (Section 2). For  $d/l > 0.36$ , the PW droplet morphology is favored, however droplet jumping is not possible due to the high solid fraction ( $\phi > 0.1$ ) and high contact line pinning to the surface structure. For  $l_c/l < 2$  (not-shown), liquid films and pinned W droplets are formed due to droplet merging within the unit cell of the structure. (b) Condensing droplet departure radius,  $\hat{R}$  as a function of coalescence length ( $l_c/l$ ) and ratio of pillar diameter to center-to-center spacing ( $d/l$ ). Regimes of W droplet formation have higher departure radii than PW droplets due to higher surface adhesion and contact angle hysteresis. Model parameters:  $h = 10 \mu\text{m}$ ,  $l = 4 \mu\text{m}$ ,  $d = 300 \text{ nm}$ ,  $\Delta T = 5 \text{ K}$ ,  $\theta_a/\theta_r = 121.6^\circ/86.1^\circ$ ,  $k_{HC} \approx 0.2 \text{ W/mK}$  [28],  $k_p = 150 \text{ W/mK}$ ,  $\delta_{HC} = 1 \text{ nm}$ . Insets: emergent droplet morphology schematics for each region.

**Figure 7** – Normalized overall steady-state surface heat flux  $q''/q_{\text{max}}''$ , as a function of coalescence length ( $l_c/l$ ) and ratio of pillar diameter to center-to-center spacing ( $d/l$ ) for (a)  $h = 5 \mu\text{m}$ , (b)  $h = 2 \mu\text{m}$ , and (c)  $h = 1 \mu\text{m}$ . Scaling down the surface structure ((a) to (c)) enhances performance due to the reduced micro/nanostructure thermal resistance. Regions favoring PW jumping droplet removal show peak heat fluxes for all three cases ((a) to (c)).  $q_{\text{max}}''$  was determined from examining the peak heat flux in all three cases, which occurred for the smallest scale structure (c),  $q_{\text{max}}'' = 342.12 \text{ kW/m}^2$ . Model parameters:  $h/l = 2$ ,  $\Delta T = 5 \text{ K}$ ,  $\theta_a/\theta_r = 121.6^\circ/86.1^\circ$ ,  $k_{HC} = 0.2 \text{ W/mK}$ ,  $k_p = 150 \text{ W/mK}$ ,  $\delta_{HC} = 1 \text{ nm}$ . Insets: emergent droplet morphology schematics for each region.

**Figure 8** – Structured surface steady-state wetting morphology as a function of the pillar diameter to center-to-center spacing ratio ( $d/l$ ) and the center-to-center spacing to pillar height ratio ( $l/h$ ). Scaling down the surface structure ( $l/h$ ) broadens the  $d/l$  regime where PW jumping droplets are observed. Insets: emergent droplet morphology schematics for each region.

**Figure 9** – Structured surface steady-state heat flux  $q''$  as a function of coalescence length  $l_c$  for four different promoter coatings with (a) coalescence-induced droplet jumping (no sweeping) and (b) gravitational droplet removal (sweeping). The surface heat flux is not sensitive to the promoter coating for surfaces with coalescence-induced droplet departure. Heat flux ( $q''$ ) is highly dependent on the promoter coating for surfaces relying on gravity for droplet removal due to the strong dependence of droplet/surface adhesion on contact angle hysteresis. Insets: Surface heat flux ( $q''$ ) as a function of temperature difference ( $\Delta T = T_{\text{sat}} - T_s$ ) for the four different promoter coatings and model parameters:  $h = 5 \mu\text{m}$ ,  $l = 2.5 \mu\text{m}$ ,  $\Delta T = 5\text{K}$ ,  $l_c = 7.5 \mu\text{m}$ ,  $k_{\text{HC}} = 0.2 \text{ W/mK}$ ,  $k_p = 150 \text{ W/mK}$ ,  $\delta_{\text{HC}} = 1 \text{ nm}$ .

**Figure 10** – Structured surface steady-state heat flux  $q''$  as a function of the surface inclination angle  $\theta$  for SAM coated (SAM1, SAM2, and THIOL) structured surfaces exhibiting coalescence-induced droplet jumping ( $d/l = 0.3$ ) and gravity based droplet shedding ( $d/l = 0.4$ ). Jumping surfaces showed little sensitivity to the orientation owing to their ability to shed droplets at length scales well below the capillary length ( $\hat{R} \ll 1 \text{ mm}$ ). Surfaces exhibiting gravity based shedding showed a strong dependence on  $\theta$ , due to the  $\cos\theta$  dependence of the gravitational body force acting on the condensing droplets needed to overcome the surface tension force (Eq. (25)). Inset: condensing surface orientation schematic. Model parameters:  $h = 5 \mu\text{m}$ ,  $l = 2.5 \mu\text{m}$ ,  $\Delta T = 5 \text{ K}$ ,  $l_c = 10 \mu\text{m}$ ,  $k_{\text{HC}} = 0.2 \text{ W/mK}$ ,  $k_p = 150 \text{ W/mK}$ ,  $\delta_{\text{HC}} = 1 \text{ nm}$ .

**Figure 11** – Structured (jumping) and flat (gravity shedding) surface steady-state heat flux  $q''$  as a function of intrinsic promoter coating contact angle hysteresis  $\Delta\theta$  for three structured surfaces coated with the SAM1 promoter. As  $\Delta\theta$  decreases for the flat surface,  $q''$  increases due to the lower droplet adhesion to the surface and lower departure radii (Inset). As a result, the flat surfaces begin to show enhanced  $q''$  compared to the structured surfaces. Inset: Droplet departure diameter ( $\hat{R}$ ), as a function of intrinsic flat surface contact angle hysteresis ( $\Delta\theta$ ). Model parameters:  $\Delta T = 5 \text{ K}$ ,  $l_c = 10 \mu\text{m}$ ,  $k_{\text{HC}} = 0.2 \text{ W/mK}$ ,  $k_p = 150 \text{ W/mK}$ ,  $\delta_{\text{HC}} = 1 \text{ nm}$ , SAM1 coating:  $\theta_a/\theta_r = 121.6^\circ/86.1^\circ$ .